

# Multi-directional Behavior of Granular Materials and Its Relation to Incremental Elasto-plasticity

Matthew R. Kuhn<sup>a,\*</sup>, Ali Daouadji<sup>b</sup>

<sup>a</sup>*Br. Godfrey Vassallo Prof. of Engrg., Donald P. Shiley School of Engrg., Univ. of Portland, 5000 N. Willamette Blvd., Portland, OR, USA 97231*

<sup>b</sup>*University of Lyon, INSA-Lyon, GEOMAS, F-69621, France*

---

## Abstract

The complex incremental behavior of granular materials is explored with multi-directional loading probes. An advanced discrete element model (DEM) was used to examine the reversible and irreversible strains for small loading probes, which follow an initial monotonic axisymmetric triaxial loading. The model used non-convex non-spherical particles and an exact implementation of the Hertz-like Cattaneo–Mindlin model for the contact interactions. Orthotropic true-triaxial probes were used in the study (i.e., no direct shear strain or principal stress rotation), with small strains increments of  $2 \times 10^{-6}$ . The reversible response was linear but exhibited a high degree of stiffness anisotropy. The irreversible behavior, however, departed in several respects from classical elasto-plasticity. A small amount of irreversible strain and contact slipping occurred for all directions of the stress increment (loading, unloading, transverse loading, etc.), demonstrating that an elastic domain, if it exists at all, is smaller than the strain increment used in the simulations. Irreversible strain occurred in directions tangent to the primary yield surface, and the direction of the irreversible strain varied with the direction of the stress increment. For stress increments within the deviatoric pi-plane, the irreversible response had rounded-corners, evidence of multiple plastic mechanisms. The response at these rounded corners varied in a continuous manner as a function of stress direction. The results are placed in the context of advanced elasto-plasticity models: multi-mechanism plasticity and tangential plasticity. Although these models are an improvement on conventional elasto-plasticity, they do not fully fit the simulation results.

*Keywords:* Granular material, plasticity, incremental response, stiffness, discrete element method

---

## 1. Introduction

The mechanical behavior of granular materials is exceedingly complex, and engineers have been challenged for decades to measure, understand, and model this complexity. The current work reveals further complexity, using discrete element (DEM) simulations to improve current understanding of the multi-directional incremental yield and flow characteristics of a material that is initially loaded under monotonic triaxial conditions. Although several frameworks have been

---

\*Corresponding to: Donald P. Shiley School of Engineering, University of Portland, 5000 N. Willamette Blvd., Portland, OR, 97203, USA. Email: kuhn@up.edu

Email addresses: kuhn@up.edu (Matthew R. Kuhn), ali.daouadji@insa-lyon.fr (Ali Daouadji)

Preprint submitted to Elsevier

August 1, 2018

developed for structuring such experimental results, including elasto-plasticity [1], hypoplasticity [2, 3], generalized plasticity [4], damage plasticity [5], micro-mechanics-based homogenization [6], endochronic [7], and shock and fracture-based [8] schema, we will place our results in the context of elasto-plasticity, which is currently the prevailing framework for rate-independent materials. Conventional elasto-plasticity is founded on six principles:

1. strain increments can be separated into distinct elastic and plastic parts as a sum or tensor product with each part being a homogeneous function of the stress increment, and with the elastic increment being a reversible function of the stress increment that is fully recovered after a closed loading–unloading cycle in stress-space;
2. the elastic increment is a linear function — both homogeneous and additive — of the stress increment;
3. the space of stress increments includes a finite elastic region within which no plastic deformation occurs;
4. the regions of elastic and plastic behavior are separated by a hyperplane (incremental yield surface) in stress-space;
5. plastic strain increments occur in a single direction, which can depend upon the current stress and its history but not upon the direction of the stress increment; and
6. the magnitude of the plastic strain is proportional to the projection of the stress increment onto the normal of the yield surface.

These principles have been tested with both laboratory experiments and simulations, in which soils or virtual assemblies of particles are loaded in small probes of stress or strain. Four laboratory programs and eleven simulation studies are summarized in Table 1. The simulation studies include the early two-dimensional (2D) studies of Bardet [11] and Alonso-Marroquín [16] and more recent three-dimensional (3D) simulations using sphere assemblies. Although laboratory tests and simulations have exposed important aspects of granular behavior, disagreement or ambiguity still remains some the principles enumerated above. Tables 2 and 3 summarize simulation results for 2D and 3D probe studies. The 2D simulations in Table 2 are limited in the range of stress-space that can be accessed, and in this sense, they are similar to 3D axisymmetric triaxial conditions, which limit the accessible space to a two-dimensional hyperplane of the principal stress components, and the 3D studies also shown in the same table. This table shows that, when tested, each of the six elasto-plasticity principles is affirmed with 2D simulations, as indicated by the “Y” cells. Some behaviors were not tested in certain studies, and these cells are left blank. Conspicuous ambiguity arises, however, in the results of 3D simulations conducted with true-triaxial conditions, in which the increments of all three principal stresses were independently varied (Table 3). For example, Tamagnini et al. [18] found that some plastic deformation, albeit small, occurred regardless of the direction of small loading probes, a result that is contrary to other 3D (and 2D) studies and to principle 3. In particular, they found that plastic strains occur for stress increments in opposite directions (i.e., for both loading and unloading), thus violating the third principle. Based upon their triaxial tests of sand, Royis and Doanh [13] also doubted the existence of a finite elastic regime, as they detected small plastic strain increments for all loading directions. Yet principle 3 was affirmed in several other studies.

In regard to principle 4, some studies have found that the elastic and plastic regions in incremental stress-space are distinct and are separated by a flat hyperplane (i.e., a yield surface

Table 1: Summary of multi-directional probe studies with laboratory tests and numerical simulations.

Study	Shape	Contacts	Method <sup>1</sup>	Probe type <sup>2</sup>	$ d\boldsymbol{\varepsilon} $ or $ d\boldsymbol{\sigma} $
Lewin & Burland [9]	shale powder	triaxial	—	—	10 kPa
Tatsuoka & Ishihara [10]	sand	triaxial	—	E–P	0.001–0.006
Bardet [11]	disks	linear	DEM	E–P	$\approx 1 \times 10^{-3}$
Anandarajah et al. [12]	sand	—	triaxial	E–P	$\approx 1 \times 10^{-4}$
Royis & Doanh [13]	sand	—	triaxial	E–P	$\approx 1 \times 10^{-4}$
Kishino [14]	spheres	linear	GEM	E–P	1 kPa
Alonso-Marroquín [15, 16]	polygons	linear	DEM	E–P	10 kPa
					$\approx 1 \times 10^{-5}$
Calvetti et al. [17, 18]	spheres	linear <sup>3</sup>	DEM	R–I	$\approx 2 \times 10^{-4}$
Sibille et al. [19]	spheres	linear	DEM	R–I	—
Plassiard et al. [20]	spheres	linear <sup>4</sup>	DEM	R–I	$\approx 2 \times 10^{-5}$
Froio and Roux [21]	disks	linear	DEM <sup>5</sup>	—	$\approx 4 \times 10^{-6}$
Harthong & Wan [22]	spheres	linear	DEM	E–P	0.1kPa
Wan & Pinheiro [23]	spheres	—	DEM	R–I & E–P	0.1 kPa
Kuhn & Daouadji [24]	sphere-clusters	linear & Hertz	DEM	R–I & E–P	$2 \times 10^{-6}$
Current work	sphere-clusters	Hertz	DEM	R–I	$2 \times 10^{-6}$

<sup>1</sup> GEM = Granular Element Method; triaxial = laboratory experiments

<sup>2</sup> R–I = reversible-irreversible; E–P = elastic-plastic (see Section 2.2)

<sup>3</sup> with rotational restraint of particles

<sup>4</sup> with rolling friction of contacts

<sup>5</sup> hybrid method: assembly loaded with DEM; probes applied with method similar to GEM [14, 25]

Table 2: Results of previous 2D simulations and their conformance with the six principles of conventional elasto-plasticity: Y = conforms with the principle, N = contradicts the principle.

Elasto-plasticity principle	Bardet [11]	Alonso-Marroquín et al. [15, 16]	Froio & Roux [21]	Sibille et al. [19]*	Plassiard et al. [20]*
(1) $d\boldsymbol{\varepsilon} = d\boldsymbol{\varepsilon}^{(e)} + d\boldsymbol{\varepsilon}^{(p)}$ , $d\boldsymbol{\varepsilon}^{(e)}$ is reversible		Y			
(2) $d\boldsymbol{\varepsilon}^{(e)}$ linear: $d\varepsilon_{ij}^{(e)} = C_{ijkl}d\sigma_{kl}$	Y	Y			Y
(3) Finite elastic domain		Y		Y	
(4) $d\boldsymbol{\varepsilon}^{(e)}$ & $d\boldsymbol{\varepsilon}^{(p)}$ domains are semi-spaces, normal $\mathbf{f}$	Y	Y	Y	Y	Y
(5) Plastic increments $d\boldsymbol{\varepsilon}^{(p)}$ in single flow direction $\mathbf{g}$	Y	Y	Y	Y	Y
(6) $ d\boldsymbol{\varepsilon}^{(p)}  = \mathbf{f} \cdot d\boldsymbol{\sigma}$	Y	Y	Y		Y

\* Three-dimensional assemblies, but with axisymmetric triaxial probes.

without corners and having unit normal direction  $\mathbf{f}$ ) [11, 15, 20, 21, 17, 19]. Other programs, however, found evidence of a possibly cornered yield surface [14, 18, 22]. Similar ambiguity is found with the assumption of a single direction of the plastic strain increment at a particular stage of loading (principle 5). In particular, Kishino [14] and Wan and Pinheiro [23] shed doubt on the fifth principle with simulations that probed a material in multiple stress directions and discovered small changes in the directions of the resulting plastic strain increments. The sixth principle, which disallows plastic strain for stress increments that lie along the yield surface (i.e., tangential increments), was refuted by Kishino [14] and Plassiard et al. [20], who detected small

Table 3: Results of previous 3D simulations and their conformance with the six principles of conventional elasto-plasticity: Y = conforms with the principle, N = contradicts the principle.

Elasto-plasticity principle	Kishino [14]	Calvetti et al. [17]	Tamagnini et al. [18]	Harthong & Wan [22]	Wan & Pinheiro [23]
(1) $d\boldsymbol{\varepsilon} = d\boldsymbol{\varepsilon}^{(e)} + d\boldsymbol{\varepsilon}^{(p)}$ , $d\boldsymbol{\varepsilon}^{(e)}$ is reversible					Y
(2) $d\boldsymbol{\varepsilon}^{(e)}$ linear: $d\varepsilon_{ij}^{(e)} = C_{ijkl}d\sigma_{kl}$	Y	Y			
(3) Finite elastic domain	Y	Y	N		
(4) $d\boldsymbol{\varepsilon}^{(e)}$ & $d\boldsymbol{\varepsilon}^{(p)}$ domains are semi-spaces, normal $\mathbf{f}$	N	Y*		N	
(5) Plastic increments $d\boldsymbol{\varepsilon}^{(p)}$ in single flow direction $\mathbf{g}$	N		N	N	N
(6) $ d\boldsymbol{\varepsilon}^{(p)}  = \mathbf{f} \cdot d\boldsymbol{\sigma}$	N	Y			

\* “Y” applies to virgin loading conditions. A finite elastic domain was not found with pre-loaded conditions.

plastic strains for these tangential increments. The conclusions of these past studies are influenced, in part, by the size of their stress or strain increments, since larger increments can obscure the existence of a cornered yield surface, the nature of the elastic domain, the character of the plastic flow directions, and the effect of a stress increment’s direction on the plastic strain increment. We also note each past study had its own particular focus, such that some of the aspects noted in Tables 2 and 3 are based upon limited data.

The current work examines each of the six principles with extensive and carefully controlled simulations that employ extremely small strain increments, a more realistic particle shape, and a rigorous implementation of Hertzian contact between particles, and we present results that more fully characterize the incremental response of a granular material — in our case, a virtual sand. We show that only the second principle survives scrutiny, yet even the linear form of the elastic response, as implied with principle 2, develops a rather extreme anisotropy that favors elastic dilation. With each principle, we more fully ascertain granular behavior and the nature of the nonconformity or agreement. The first principle was the focus of a second article by the authors [24], which demonstrated that elastic strain increments, although recoverable, are not reversible, a finding that is more fully described below in the context of elastic-plastic coupling [26, 27]. As such, the elastic–plastic partition of strain increments — the basis of the first principle — is replaced with a reversible–irreversible partition, and the terms “reversible” and “irreversible”, defined below, will replace elastic and plastic in this work (see also [28, 29]).

Because the simulations demonstrate a lack of conformity with five of the six principles, we also consider more advanced elasto-plastic models, which allow a softer response in certain directions and restrict the zone of elastic behavior: generalized plasticity [30], multi-mechanism plasticity [31], and tangential plasticity [4, 32]. These models were originally developed to explain the susceptibility of materials to certain localized failure modes, and their success in modeling our simulation results is quite remarkable, considering that they were originally based upon very sparse evidence of the behavior of these materials.

The plan of the paper is as follows. In the following section, we review the application of discrete element simulations for modeling incremental behavior, present the particular features of the model used in the current work, and discuss the alternative separations of strain increments with elastic–plastic and reversible–irreversible partitions. In Section 3, we review our results of several series of stress probes that test the six principles of elasto-plastic materials set forth above. The nature of the measured reversible and irreversible strains are then critically examined in Sections 4 and 5. Because of inconsistencies between the simulation results and conventional

elasto-plastic theory, we assess two modest extensions of the theory — multi-mechanism and tangential plasticity — and evaluate their fit with the simulations.

## 2. DEM Modeling

DEM simulations have become an important means for characterizing the directional yield and flow properties for small increments of loading and to decompose the resulting strain increments into reversible and irreversible (or elastic and plastic) parts. Simulations, both past and current, are meant to augment understanding of granular materials gained from physical tests. However, because micro-scale information and more general boundary conditions are accessible with DEM simulations, they can expose granular behavior in ways that are not easily achieved with laboratory testing. Specifically, three advantages of DEM simulations were exploited in our simulations. First, after creating a granular assembly and loading it monotonically to a given state, this state and all of its micro-data are saved. This saved state — which Alonso-Marroquín [16] calls a numeric “clone” — constitutes a consistent reference state for subsequent loading probes. Second, in performing the loading probes, the DEM code permitted control of arbitrary combinations of six components of the stress and strain tensors or any six linearly independent combinations of stress and strain — loading conditions that would require multiple sample preparations and even different testing apparatus in a physical laboratory [33]. Finally, by using different variations of probes, described in Section 2.2, we measured the separate reversible and irreversible constituents of the total strain increments. Because of these and other advantages, simulations have begun to supplant physical experiments for investigating certain aspects of granular behavior.

### 2.1. DEM model and monotonic triaxial compression

We used a series of slow, quasi-static DEM simulations to study the multi-directional incremental response of a granular assembly (model details are described in Appendix A). Unlike the dynamic regime of behavior, in which shock waves can move through the material [34, 35], our slow strain rate assures that particles remain in near-equilibrium and that results are independent of the loading rate. The assembly was a cubical box filled with 10,648 smooth non-convex sphere-cluster particles contained within periodic boundaries. The particles’ non-convex shapes were intended to capture the irregular shapes of sand particles, which permit the nestling of particle pairs that share multiple contacts. The shape, sizes, and arrangement of the particles were calibrated to closely simulate the behavior of the fine-grain poorly-graded medium-dense Nevada Sand (see the Appendix and [36]). The assembly was large enough to capture the average material behavior but sufficiently small to prevent meso-scale localization, such as shear bands [37, 23]. A distinctive feature of sands is the dependence of the elastic moduli upon the confining (mean) stress. To capture this behavior, the contacts between particles were modeled with a Hertz normal response and a full implementation of the Cattaneo–Mindlin tangential response, which permits slip, micro-slip, and elastic behaviors at the contacts [38, 39]. To model such non-linear contact behavior, most DEM studies use an approximation of the Cattaneo–Mindlin contact, with the tangential stiffness taken as a multiple of the normal stiffness, which changes with the normal force. This common approximation can produce an unintended infusion of energy during a closed cycle of contact loading [40]. Because we relied upon loading-unloading probes, we deemed an energetically-consistent full implementation of the Cattaneo–Mindlin contact as essential for determining the incremental stiffness characteristics of granular materials (Appendix A). The dense initial particle arrangement was isotropic with a confining (negative mean) stress of 100 kPa

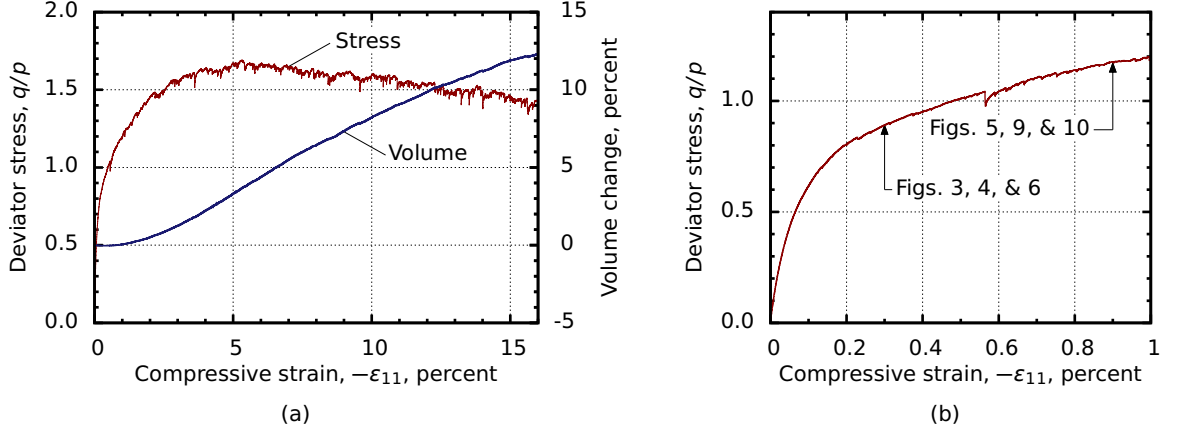


Figure 1: Stress, strain, and volume change during DEM simulation of triaxial compression at a constant mean stress of 100 kPa.

and porosity 0.363 (void ratio of 0.570). During subsequent loading, the inter-particle friction coefficient was 0.55.

Although it is inconsistent with the quasi-static hypothesis, DEM results can depend upon the loading rate — an unfortunate dependence which is infrequently discussed in a candid manner in the DEM literature. (Such rate effects have, for decades, been recognized in laboratory soil testing, and measures are usually taken to reduce these effects, e.g., [9].) To mitigate such rate dependence, a slow loading rate and other measures were taken, assuring that the simulations were nearly quasi-static. Because of their importance in the current study, computational essentials are detailed in Appendix A, which also describes quantitative indicators verifying the rate-independent, quasi-static nature of the simulations.

The loading conditions in this study were orthotropic with no transverse shearing, so that the principal stress and strain rates did not rotate during deformation, obviating the need to resolve non-coaxial behavior or distinguish between a co-rotated stress rate and the simpler Cauchy rate  $\dot{\sigma}$ . Figure 1 shows the results of drained isobaric (constant- $p$ ) axisymmetric triaxial compression, in which the  $x_1$  width of the assembly was reduced at constant rate  $\dot{\epsilon}_{11}$ , while adjusting the lateral widths to maintain a constant mean stress of 100 kPa. The lateral stresses,  $\sigma_{22}$  and  $\sigma_{33}$ , were maintained nearly equal during this monotonic constant- $p$  compression, with ( $\sigma_{22} \approx \sigma_{33}$ , see Appendix A for verification of the careful control of stresses during monotonic loading and stress probes). In the figure, the deviator stress  $q$  is the negative of  $\sigma_{11} - \frac{1}{2}(\sigma_{22} + \sigma_{33})$ , and pressure (negative mean stress)  $p = -\frac{1}{3}(\sigma_{11} + \sigma_{22} + \sigma_{33})$ . All of the subsequent stress probes began from initial states taken along this path of monotonic axisymmetric loading.

## 2.2. Stress probe methods

The separation of strain increments into elastic and plastic parts is an established concept in constitutive modeling, and the part of a strain increment that is recovered after completing a closed loading–unloading cycle in stress-space is usually assumed to be free of contact slip; whereas, the remaining, permanent part of a strain increment is usually associated with frictional dissipation during such closed cycles. Collins and Houlsby noted, however, that recoverable (elastic) strain increments might not be entirely dissipation-free (reversible), and permanent

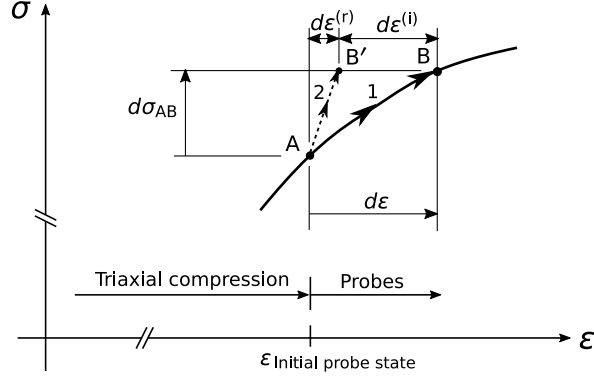


Figure 2: Probes AB and AB' to determine the total and reversible strain increments.

(plastic) strain increments might not be purely dissipative (irreversible, see also [41]). Hueckel [26, 28, 42] noted that the micro-structure of a material can be altered by internal changes that accompany plastic deformation, and that these internal changes produce modifications of the elastic moduli concurrently with the loading (termed *elastic-plastic coupling*). These internal changes, tracked perhaps with internal variables [27], accompany dissipation but can be caused by processes that are, themselves, dissipation-free. Pouragha and Wan [43, 44] have noted that the creation and disintegration of contacts and geometrical alterations of the contact arrangement, which occur during deformation, are such non-dissipative mechanisms that can alter the elastic moduli with loading. The distinction between elastic and reversible strain increments must, therefore, be considered when planning incremental probes, as different DEM techniques are available for determining the elastic–plastic and reversible–irreversible partitions of a strain increment. The authors have used both techniques and found small differences in the resulting partitions, demonstrating the existence of elastic–plastic coupling and contradicting the principle 1 of conventional elasto-plasticity [24]. These DEM results differ from those of Wan and Pinheiro [23], who found an equivalence of the reversible and elastic strains. Although the reversible–irreversible partition can not be ascertained in a laboratory setting, this partition is considered more fundamental, and it was shown to produce a more regular separation of the incremental response (for example, a linear stiffness relationship between increments of stress and reversible strain).

For these reasons, we have measured the reversible and irreversible strains — in both magnitude and direction — by using a DEM technique pioneered by Calvetti and his co-workers [18]. The initial, reference states for our series of probes were first established during the course of drained monotonic axisymmetric isobaric (constant- $p$ ) triaxial compression (Fig. 1). At several reference strains, we fully saved the status of all particles and contacts, so that different deformation probes could be started from these “initial probe states” (point A in Fig. 2). Starting at an initial probe state, each probe was begun by advancing strain in a particular direction to produce a strain increment of magnitude  $|d\epsilon| = 2 \times 10^{-6}$  (the increment AB in Fig. 2), where the norm  $|d\epsilon| = \sqrt{d\epsilon_{11}^2 + d\epsilon_{22}^2 + d\epsilon_{33}^2}$ . At the end of this probe (point B), we noted the resulting increments of all strain and stress components during this initial probe. To determine the reversible part of this deformation, we conducted a dissipation-free “reversible probe” (AB' in Fig. 2) by replicating the same *stress increment* as during loading (the increment  $d\sigma_{AB}$ ) but computationally preventing contact slip (and micro-slip) by assigning a large friction coefficient (i.e.,  $\mu = 50$ ).

That is, we first determined the stress increment  $d\sigma_{AB}$  that resulted from unadulterated loading with a contact friction coefficient  $\mu = 0.55$ , and then we produced this same stress increment with  $\mu = 50$ . The latter strain increments were free of contact slip and were entirely the result of elastic contact movements: these strain increments are the reversible strains  $d\epsilon^{(r)}$ , and the irreversible strains  $d\epsilon_{ij}^{(i)}$  are the difference  $d\epsilon_{ij} - d\epsilon_{ij}^{(r)}$ . We note, again, that the reversible strain is not the “recoverable strain,” as irreversible processes in the form of contact slip, contact micro-slip, and particle rearrangement occur at all stages and in all directions of a loading–unloading cycle in stress-space. The technique for isolating the reversible part of a strain increment was used in [24] to demonstrate that granular materials exhibit elastic–plastic coupling and that during strain hardening, contact slip — a distinctly irreversible mechanism — accompanies loading in any direction. Another irreversible mechanism, the non-dissipative gain and loss of contacts, can also occur during deformation [43], and this mechanism was not precluded in the AB’ probes. As such, our technique of measuring the reversible–irreversible partition involves an unavoidable approximation. We note, however, that contact loss and gain was rarely observed during the strain increments of  $2 \times 10^{-6}$ .

### 3. Multi-direction stress probes

Stress and strain probes were used to characterize yield and flow for loading in multiple directions, a purpose for which the advantages of DEM simulations are most persuasive. The current work extends the studies in Table 1 by conducting a comprehensive series of probes that cover the three-dimensional space of incremental principal stress. We also submit the results to a close scrutiny that reveals new phenomena and insights of the elasto-plastic behavior of granular materials. The probe strains are of size  $2 \times 10^{-6}$ , much smaller than previous studies, and the current simulations differ in several other respects from past studies: the use of non-convex sphere-clusters, an exact Hertz-like Cattaneo–Mindlin contact model, and the slow loading necessary to produce quasi-static conditions.

#### 3.1. Framework of generalized stress and strain

We conducted several series of incremental probes in the three-dimensional space of normal strains,  $[\epsilon] = [\epsilon_{11}, \epsilon_{22}, \epsilon_{33}]^T$ , and in the complementary space of normal stresses,  $[\sigma] = [\sigma_{11}, \sigma_{22}, \sigma_{33}]^T$ , where extensional strains and tensile stresses are positive. Because the 3D rectangular assembly was not sheared and only rectilinear deformations were applied, these normal components are the principal strains and stresses that fully express the deformation and loading conditions. An assembly was first loaded in constant- $p$  triaxial compression to an initial probe state (Fig. 2), and the subsequent probes were true-triaxial increments of the strain and stress increments,  $[d\epsilon]$  and  $[d\sigma]$ . Rather than express the results in Lode coordinates or principal strain coordinates, we normalize and plot the deviatoric and volumetric components of these increments in a systematic manner, by transforming the Cartesian components of strain into an alternative set of generalized components, for which the unit vectors  $\vec{e}_1$ ,  $\vec{e}_2$ , and  $\vec{e}_3$  serve as an orthonormal basis, organized as the columns of a matrix  $[\mathbf{E}]$ ,

$$[\mathbf{E}] = [\vec{e}_1, \vec{e}_2, \vec{e}_3] = \left[ \frac{-1}{\sqrt{3}} \begin{bmatrix} 1 \\ 1 \\ 1 \end{bmatrix}, \frac{-1}{\sqrt{2}} \begin{bmatrix} 0 \\ 1 \\ -1 \end{bmatrix}, \frac{-1}{\sqrt{6}} \begin{bmatrix} 2 \\ -1 \\ -1 \end{bmatrix} \right] \quad (1)$$



When represented in the three-dimensional space of Cartesian (principal) strains,  $\varepsilon_{11}$ ,  $\varepsilon_{22}$ , and  $\varepsilon_{33}$ , these basis vectors have the following meanings:  $\vec{e}_1$  is the compressive volumetric direction;  $\vec{e}_2$  is a transverse-deviatoric direction perpendicular to the Rendulic plane (i.e., perpendicular to the plane of volume strain  $v$  and strain  $\varepsilon_{11}$ ); and  $\vec{e}_3$  is the deviatoric direction that would be accessible by axisymmetric triaxial conditions, within the Rendulic plane. Because matrix  $[\mathbf{E}]$  is orthonormal, the conventional strain  $[\varepsilon]$  and stress  $[\sigma]$  can be scaled and expressed in the new basis vectors with the generalized scalar components  $[e_1, e_2, e_3]^T$  and  $[s_1, s_2, s_3]^T$ :

$$[\varepsilon] = e_1 \vec{e}_1 + e_2 \vec{e}_2 + e_3 \vec{e}_3, \quad [\varepsilon] = [\mathbf{E}][\mathbf{e}], \quad \text{and} \quad [\mathbf{e}] = [\mathbf{E}]^T [\varepsilon] \quad (2)$$

$$[\sigma] = s_1 \vec{s}_1 + s_2 \vec{s}_2 + s_3 \vec{s}_3, \quad [\sigma] = [\mathbf{E}][\mathbf{s}], \quad \text{and} \quad [\mathbf{s}] = [\mathbf{E}]^T [\sigma] \quad (3)$$

(note the lack of an over-arrow with the scalar lists  $[\mathbf{e}]$  and  $[\mathbf{s}]$ ). Henceforth, we refer to the 1–2–3 components as volumetric, transverse-deviatoric, and deviatoric, respectively, and we refer to the Rendulic plane, the pi-plane, and the transverse-orthogonal plane as planes with  $e_2 = 0$ ,  $e_1 = 0$ , and  $e_3 = 0$ , respectively [45]. Note that volume strain  $e_1$  and isotropic stress  $s_1$  are compressive.

The term “tangential” has been applied to stress increments that are orthogonal to the *normal of the yield surface* (direction  $\mathbf{f}$  in Section 5) [4]. For the axisymmetric condition of our initial triaxial compression, the yield surface normal should lie within the  $\vec{s}_1$ – $\vec{s}_3$  plane (the Rendulic plane), and the  $\vec{s}_2$  direction should be orthogonal to (tangential to) the yield normal. The full tangent plane will also include components in the  $\vec{s}_1$  and  $\vec{s}_3$  directions. The generalized stresses and strains of Eqs. (2)–(3) are work-conjugate and are particularly convenient for planning, plotting, and analyzing the results of simulation probes.

### 3.2. Results of strain and stress probes

In this section, we describe the primary trends of the reversible and irreversible strain increments that were measured with probes that started from an initial stage of constant- $p$  triaxial compression (Fig. 1). Three series of probes were conducted: probes within each of the three planes  $\vec{e}_1$ – $\vec{e}_2$ ,  $\vec{e}_1$ – $\vec{e}_3$ , and  $\vec{e}_2$ – $\vec{e}_3$  of generalized strain or stress. Figure 3 shows the results of deviatoric probes in the octahedral pi-plane,  $\vec{e}_2$ – $\vec{e}_3$ , for probes that were either isochoric or isobaric, and each sub-figure is a plane of incremental strain,  $de_2$  and  $de_3$ , or of incremental stress,  $ds_2$  and  $ds_3$ . The conditions of this figure could be accessed, for example, with true-triaxial equipment in a laboratory setting. Continued axisymmetric triaxial compression is in the upward direction of these figures, and a reversal of triaxial compression (unloading or triaxial extension) is downward. The probes in Fig. 3 were conducted during the early stage of strain hardening, at the reference strain  $\varepsilon_{11} = -0.3\%$ , for which the deviator stress was about 55% of the peak strength (see Fig. 1b). Each sub-figure is the result of at least eighty probes.

Figure 3a shows the magnitudes of the changes in stress  $d\sigma$  that resulted from isochoric (undrained) strain probes that shared a deviatoric strain magnitude,  $|d\varepsilon| = \sqrt{d\varepsilon_{11}^2 + d\varepsilon_{22}^2 + d\varepsilon_{33}^2} = 2 \times 10^{-6}$ . That is, Fig. 3a shows the locus of stress increments  $[ds_2, ds_3]^T$  produced by strain probes with an equal Euclidean magnitude of the deviatoric strain increment  $[de_2, de_3]^T$ . As expected, the behavior is softer (smaller radial distances) in the direction of continued triaxial compression (upward) than for triaxial unloading (downward).

Figure 3b gives additional results for deviatoric isochoric strain probes with an equal magnitude of strain (radius  $2 \times 10^{-6}$  of the total strain circle). The reversible and irreversible strains were determined with the method described in the previous section and illustrated in Fig. 2, and Fig. 3b gives the loci of the irreversible and reversible strain increments that were produced by probes of equal strain magnitude  $|d\varepsilon|$ . The irreversible strain increment  $d\varepsilon_{ij}^{(i)}$  was the largest part the

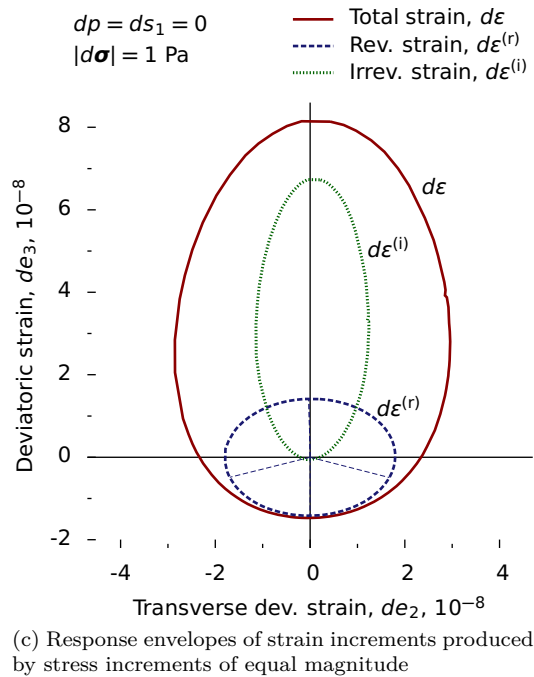
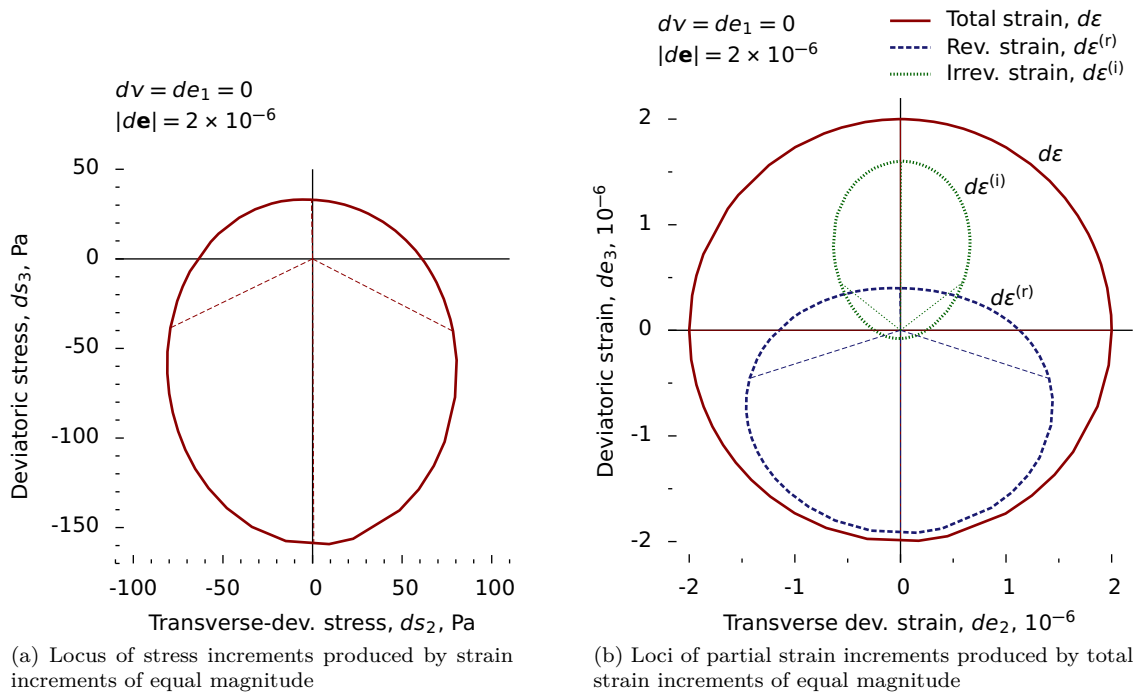


Figure 3: Pi-planes of deviatoric strain-probes, conducted at the reference strain  $\varepsilon = -0.3\%$ : (a) locus of stress increments produced with deviatoric strain increments of equal magnitude under undrained, isochoric conditions; (b) loci of reversible and irreversible strain parts, for total strain increments of equal magnitude under undrained, isochoric conditions; and (c) response envelopes of strain increments that resulted from deviatoric stress increments of equal magnitude under isobaric (drained, constant- $p$ ) conditions.

total strain increment when the probe was in the direction of continued triaxial compression (upward in the figure); whereas, reversible strain increment  $d\epsilon_{ij}^{(r)}$  was the largest part for triaxial unloading (downward) and for neutral (horizontal) probes that produced transverse-deviatoric strains in direction  $d\bar{\epsilon}_2$ . A careful inspection of Fig. 3b reveals that a small irreversible strain is also produced in the downward “unloading” direction of triaxial extension, a result that was also mentioned by Tamagnini et al. [18] and is explored more fully below.

Figure 3c shows the reversible and irreversible parts of strain increments that were produced by deviatoric *isobaric* stress probes having an equal incremental stress magnitude of 1 Pa (i.e., a magnitude  $|d\sigma| = |ds| = \sqrt{ds_1^2 + ds_2^2 + ds_3^2} = 1$  Pa). Each probe had a strain magnitude of  $2 \times 10^{-6}$ , and after noting the resulting stress increment, the strain was scaled to the stress magnitude of 1 Pa. Like the response envelopes of Gudehus [46], this figure displays the strain increments produced by stress increments that share an equal magnitude but are applied in different directions. The irreversible response in Fig. 3c is not a straight line but has a narrow elliptic shape, an indication that, contrary to conventional elasto-plasticity (principle 5), a single flow direction does not apply to granular materials. Our results are similar to those of Kishino [14], Tamagnini et al. [18], and Wan and Pinheiro [23], although the irreversible response envelopes in these earlier studies had a tear-drop shape instead of the elliptic shape of our simulations (see also [47] for a discussion). The dependence of flow direction on loading direction is more fully described in Section 5.

The incremental response to deviatoric and *volumetric* loading is shown in Fig. 4 with Rendulic diagrams of the incremental strains,  $de_1$  and  $de_3$ , and of the incremental stresses,  $ds_1$  and  $ds_3$ . The conditions depicted in this figure could be accessed with conventional axisymmetric triaxial loading equipment (e.g., the studies in Table 2). As with the previous figure, the initial probe state of this figure is at a reference strain  $\epsilon_{11} = -0.3\%$ . At this strain, the deviator stress was about 55% of the peak strength, and the volumetric behavior was slightly dilative, as the neutral condition of zero volume strain had occurred at an earlier strain of 0.2%. In the figure, continued triaxial compression is upward; a reversal of triaxial compression (triaxial extension) is downward; isotropic compression is to the right; and expansion (dilation) is to the left.

Radial distances in Fig. 4a are the magnitudes of the stress increments that were produced by equal magnitudes of strain  $|d\epsilon| = |de| = 2 \times 10^{-6}$ . As expected, the behavior is stiffer for volumetric increments than for deviatoric increments and is softer for continued deviatoric loading (upward) than for deviatoric unloading (downward). Figure 4b shows magnitudes of the reversible and irreversible parts of the strain increments that were produced by equal magnitudes of total strain: each curve is a locus of increments,  $de_1$  and  $de_3$ , for an equal magnitude of the *total* strain increment (over eighty probes are represented). At the early stage of strain hardening represented in this figure, both reversible and irreversible strains are of comparable magnitude. Note that the locus of reversible strain magnitude crosses that of the total strain, an unusual result that is consistent with the triangle inequality,  $|d\epsilon^{(r)}| + |d\epsilon^{(i)}| \geq |d\epsilon|$ .

In Fig. 4c, we show the deviatoric–volumetric response envelopes for equal-magnitude *stress increments*,  $|d\sigma| = |ds| = 1$  Pa. Each probe had a strain magnitude of  $2 \times 10^{-6}$ , and after noting the resulting stress increment, the strain was scaled to the stress magnitude of 1 Pa. The elliptical shape of the response envelope of reversible strain indicates a greater reversible stiffness for volumetric than for deviatoric loading, and the ellipse’s tilt is evidence of a coupling of volumetric and deviatoric strains through the Poisson effect. The irreversible strain appears as a nearly straight line that radiates from the origin, indicating a single direction of the irreversible strain when viewed in the Rendulic plane, a result similar to the simulations in Table 2 and the soil experiments of Anandarajah et al. [12], Royis and Doanh [13], and Darve and Nicot [47].

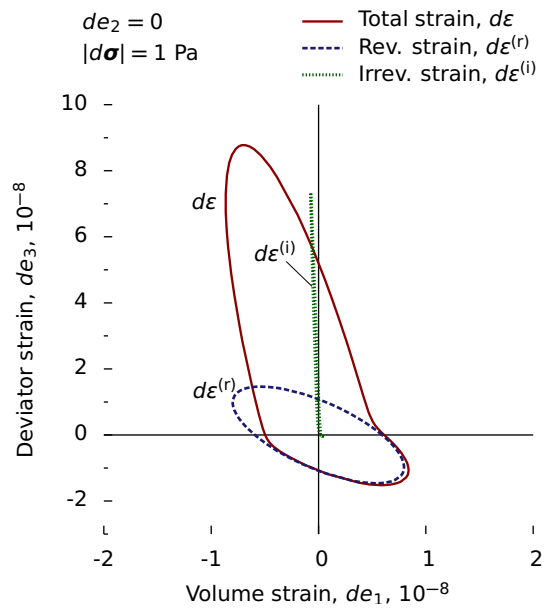
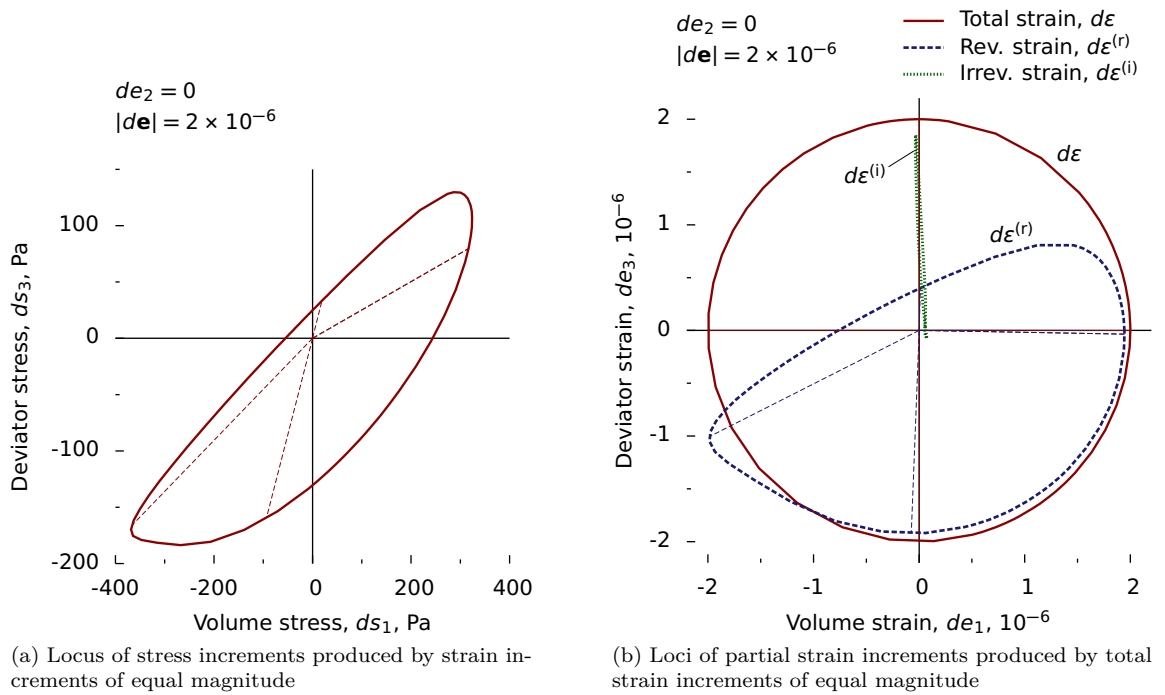


Figure 4: Results of strain probes in the Rendulic volumetric–deviatoric plane, conducted at the strain  $\varepsilon_{11} = -0.3\%$ : (a) locus of stress increments produced by strain increments of equal magnitude; (b) loci of reversible and irreversible strain parts, for total strain increments of equal magnitude; and (c) response envelopes of strain increments that resulted from volumetric–deviatoric stress increments of equal magnitude, 1 Pa.

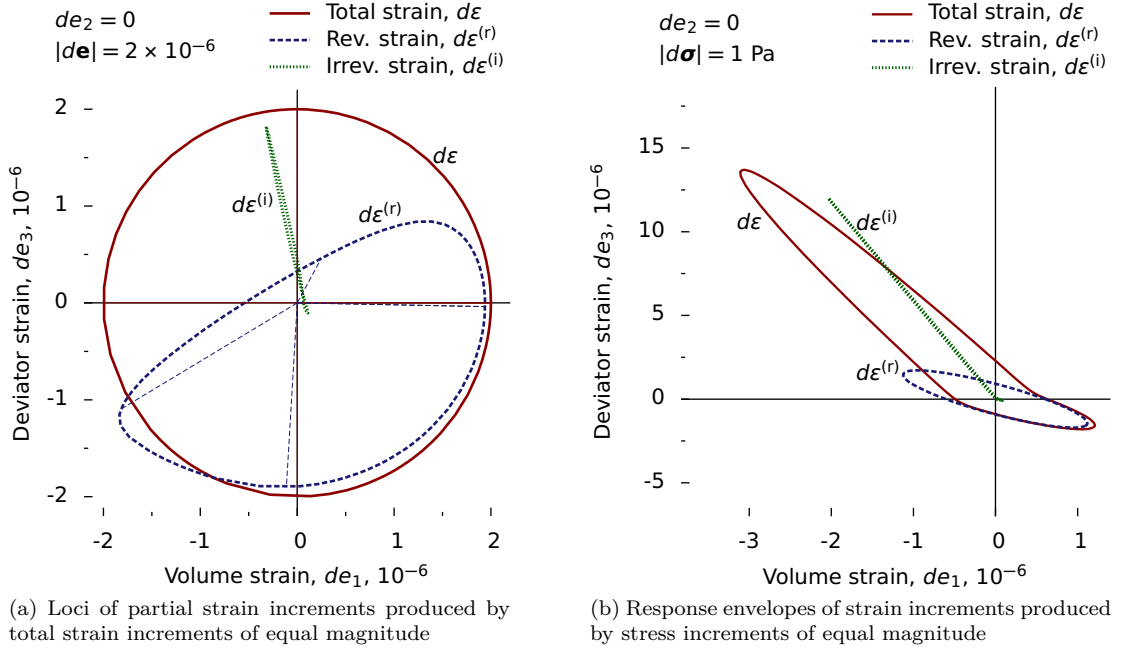


Figure 5: Results of strain probes in the Rendulic volumetric–deviatoric plane, conducted at the strain  $\varepsilon_{11} = -0.9\%$ : (a) loci of volumetric and deviatoric parts for total strain increments of equal magnitude; and (b) response envelopes of strain increments that resulted from volumetric–deviatoric stress increments with an equal stress magnitude of 1 Pa.

The irreversible strain is predominantly deviatoric, but with a slight tilt due to a small dilation tendency.

Figure 5 shows similar results within the Rendulic plane but at a more advanced stage of loading. At the reference strain  $\varepsilon_{11} = -0.9\%$  the material is still hardening, but the stress has advanced to 78% of the peak strength (see Fig. 1). The strain contributions in Fig. 5a are for total strain increments of equal magnitude ( $2 \times 10^{-6}$ , as in Fig. 4b), and the dilation tendency of the irreversible strain is more pronounced than at the lower strain (as in Fig. 4c), with an upward slope toward the left. The response envelopes in Fig. 5b are for strain increments that produce equal-magnitude increments of stress. These results can be compared with those in Fig. 4d for the earlier strain, as the axes of the two figures share the same aspect ratio. The larger dilation tendency of irreversible strain is clearly expressed in Fig. 5. The regular, elliptic shape of the reversible strain suggests a linear relationship between the tensors of incremental strain and stress, and the more pinched shape of the ellipse indicates a greater anisotropy of the reversible moduli.

The transverse-orthogonal planes in Fig. 6 are of probes in which stress increments were confined to the  $\vec{s}_1$ – $\vec{s}_2$  plane of volumetric and transverse-deviatoric directions, a type of result not yet reported in the literature. As with the previous Figs. 3 and 4, this figure is for an initial probe state of  $\varepsilon_{11} = -0.3\%$ , at which the material had attained 55% of its peak strength. The magnitudes of the total strain increments were  $2 \times 10^{-6}$  for the results in Fig. 6a; whereas, the magnitudes of the stress increments were 1 Pa for the response envelopes in Fig. 6b. Unlike previous figures, the locus of total strain in Fig. 6a is not a circle, since loading was confined to *stress* within the  $\vec{s}_1$ – $\vec{s}_2$  plane, and some out-of-plane (deviatoric) strains accompanied the

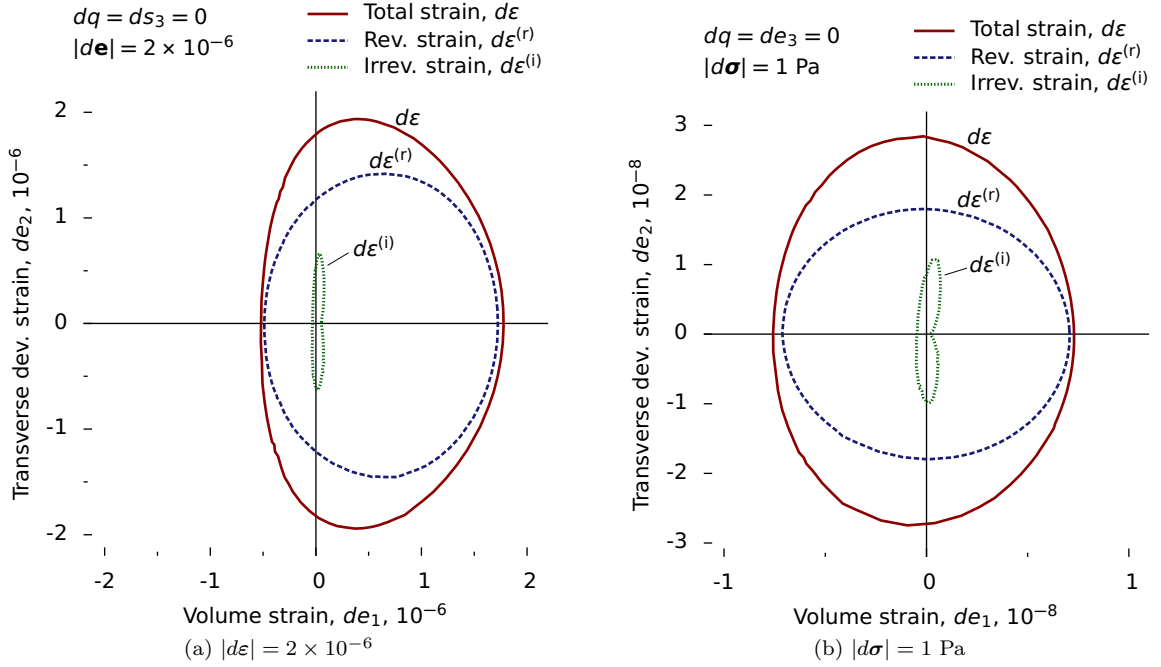


Figure 6: Strains for stress probes in the plane of volumetric and transverse-deviatoric stress (transverse-orthogonal planes), conducted at the strain  $\varepsilon_{11} = -0.3\%$ : (a) loci of volumetric and transverse-deviatoric strains for total strain increments of equal magnitude; and (b) response envelopes of strain increments that resulted from volumetric and transverse-deviatoric stress increments with an equal stress magnitude of 1 Pa.

in-plane strains of the figure (contrarily, with Figs. 3b, 4b, and 5a, *strains* were confined to their respective planes). The most notable feature of this figure is the significant irreversible strain that occurs in the *transverse-deviatoric direction*. In conventional plasticity with a single yield surface, the surface should pass through the  $\vec{s}_2$  vertical axes of Fig. 6 for the axisymmetric conditions produced by the initial triaxial loading, and instead of a loop, the irreversible response  $d\varepsilon^{(i)}$  should be a single point at the origin of these plots. The vertical transverse-deviatoric irreversible strains in this figure are *tangent* to (and lie within) the conventional yield surface, and the occurrence of non-zero strains in this tangent direction is one of several deviations from conventional plasticity that are addressed in Section 5. As with the other series of probes, the reversible response envelope in Fig. 6b is an almost perfect ellipse.

#### 4. Analysis of reversible strains

We now separately analyze the reversible and irreversible strain increments from at least 240 probes at each of several strains during the initial phase of constant- $p$  triaxial compression. The strain increments are analyzed in the context of conventional elasto-plasticity, with the reversible strains being analyzed in the current section. The elliptic shape of the reversible response envelope in Fig. 3c is evidence of anisotropy in the reversible stiffness, as the ellipse of reversible strain would appear as a circle for an isotropic material. Many of the studies listed in Tables 1–2 had also found the elastic (or reversible) response envelope to be modestly elliptical [11, 16, 17, 20, 19].

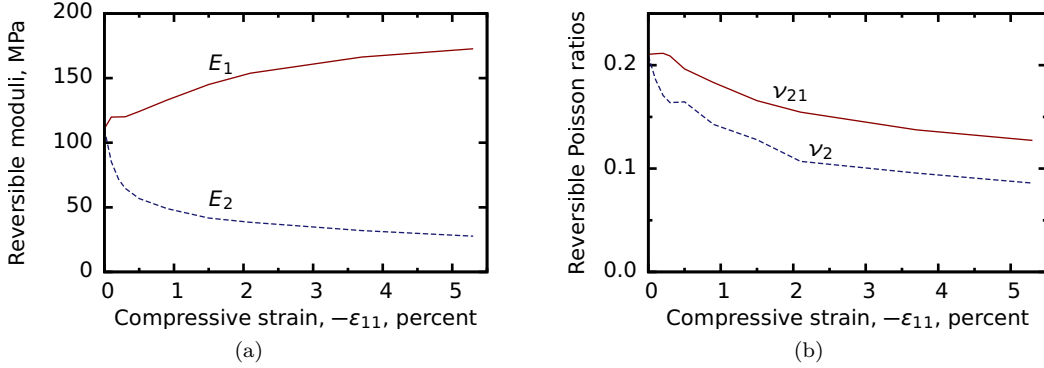


Figure 7: Reversible moduli and Poisson ratios for constant- $p$  triaxial compression.

Because our assembly began with an isotropic stress and an isotropic fabric before undergoing the initial monotonic axisymmetric triaxial compression, we would expect transverse isotropy to be induced in the stiffness. If so, the reversible strain  $d\boldsymbol{\varepsilon}^{(r)}$  should have a linear incremental form, with reversible compliance operator  $\mathcal{C}^{(r)}$ , as

$$[d\boldsymbol{\varepsilon}^{(r)}] = \mathcal{C}^{(r)}(d\boldsymbol{\sigma}), \quad \begin{bmatrix} d\varepsilon_1^{(r)} \\ d\varepsilon_2^{(r)} \\ d\varepsilon_3^{(r)} \end{bmatrix} = [\bar{\mathbf{C}}] \begin{bmatrix} d\sigma_1 \\ d\sigma_2 \\ d\sigma_3 \end{bmatrix}, \quad [\bar{\mathbf{C}}] = \begin{bmatrix} 1/E_1 & -\nu_{21}/E_2 & -\nu_{21}/E_2 \\ -\nu_{12}/E_1 & 1/E_2 & -\nu_2/E_2 \\ -\nu_{12}/E_1 & -\nu_2/E_2 & 1/E_2 \end{bmatrix} \quad (4)$$

and as a further condition of transverse isotropy,  $\nu_{21}/E_2 = \nu_{12}/E_1$ , leaving four independent parameters: the two moduli,  $E_1$  and  $E_2$ , and the two Poisson ratios,  $\nu_{21}$  and  $\nu_2$ .

We computed best-fit values of the reversible compliance  $[\bar{\mathbf{C}}]$  for a range of initial probe states: from the initial isotropic assembly ( $\varepsilon_{11} = 0$ ) to the strain at peak strength ( $\varepsilon_{11} = -5.3\%$ , Fig. 1). At each strain, we used the results of over two hundred stress-controlled probes within each of the three orthogonal planes,  $\bar{\mathbf{e}}_1-\bar{\mathbf{e}}_2$ ,  $\bar{\mathbf{e}}_1-\bar{\mathbf{e}}_3$ , and  $\bar{\mathbf{e}}_2-\bar{\mathbf{e}}_3$ . The best-fit was a projection of the simulation data — the generalized increments  $[ds]$  and  $[de]$  — onto the nine-dimensional space of the components of the generalized compliance matrix  $[\mathbf{C}]$ , such that  $[de] \approx [\mathbf{C}][ds]$ . The Cartesian components of  $[\bar{\mathbf{C}}]$  were then computed as  $[\bar{\mathbf{C}}] = [\mathbf{E}][\mathbf{C}][\mathbf{E}]^T$ .

Figure 7 summarizes the reversible moduli and Poisson ratios at eight strains during constant- $p$  triaxial compression. Starting from an isotropic condition, anisotropy was soon expressed at the smallest strain for which the compliances were computed ( $\varepsilon_{11} = -0.1\%$ ). The axial modulus  $E_1$  increased modestly from values of 111 MPa to 173 MPa across the range of strains. The greatest change, however, was in the lateral modulus  $E_2$ , which severely degraded from 111 MPa to 28 MPa. As such, the ratio of stiffnesses,  $E_1/E_2$ , increased throughout loading, reaching a ratio greater than 6 at the peak strength. The Poisson ratios  $\nu_{21}$  and  $\nu_2$  were reduced across the range of strains (Fig. 7b).

These results can be interpreted in the context of the volumetric effects that are typically observed during monotonic triaxial loading of sands. The three most common laboratory conditions are triaxial compression with constant lateral stress ( $\varepsilon_{11} < 0$ ,  $d\sigma_{22} = d\sigma_{33} = \text{constant}$ ), constant- $p$  triaxial compression ( $\varepsilon_{11} < 0$ ,  $p = \text{constant}$ ,  $\varepsilon_{22} = \varepsilon_{33}$ ), and undrained (isochoric) triaxial compression ( $\varepsilon_{11} < 0$ ,  $dv = de_3 = 0$ ,  $\varepsilon_{22} = \varepsilon_{33}$ ).

1. With the first type of laboratory procedure, the volume change of sand is typically negative

(contractive) at the start of loading but can transition to positive (dilative) during the course of loading, and is most dilative near the peak strength. The stiffness anisotropy that was induced by the triaxial loading of our simulations (Fig. 7) is consistent with these trends, as the ratio of *reversible* volume change,  $dv^{(r)}/(-\varepsilon_{11}^{(r)}) = 2\nu_{21}E_1/E_2 - 1$ , was  $-0.58$  (contractive) at the start of loading, transitioned to a neutral rate of zero at a strain of about 0.9%, and was 0.59 (dilative) at the strain of 5.3%, at the peak strength.

2. The results of our constant- $p$  simulations are similar to those of laboratory tests on medium dense sands: the measured rate of volume change was zero at the start of loading, was negative for strains between 0 and 0.2%, but became dilative at larger strains and was strongly positive at the peak strength. The reversible moduli are consistent with these results, with a reversible rate of volume change  $dv^{(r)}/(-\varepsilon_{11}^{(r)}) = 3(1 - \nu_2 + \nu_{21} - E_2/E_1)/(1 - \nu_2 + \nu_{21} + 2E_2/E_1)$  that was zero at the start of loading and become strongly dilative ( $= 3.1$ ) at the peak strength.
3. With laboratory undrained (isochoric) triaxial compression tests of sands, the mean stress typically changes as the specimen is being loaded. Except for very densely packed specimens, the mean stress typically decreases at the start of loading and can either continue to decrease (contractive behavior) or begin to increase (dilative behavior) at larger strain. For the reversible moduli in Fig. 7, the rate of change of the mean stress  $dp/(-d\varepsilon_{11})$  would be negative at the start of loading, but would transition to a positive rate at a strain of less than 0.1% and then continue to increase during loading.

These trends in reversible volumetric behavior result from the anisotropies of stiffness that were induced by the initial monotonic loading, and for each type of laboratory test, a contractive or dilative tendency can be attributed, at least partially, to the induced anisotropy of the reversible stiffness. These trends, of course, are of the *reversible rates*, the ratio  $dv^{(r)}/(-d\varepsilon_{11}^{(r)})$ , computed from the reversible moduli and Poisson ratios, rather than a total rate  $dv/(-d\varepsilon_{11})$  that includes both reversible and irreversible strains. The irreversible strains are analyzed in the next section.

To complete the analysis of reversible behavior, we considered the possible asymmetry of the reversible compliance matrix  $[\bar{\mathbf{C}}]$ . The Poisson ratios that are plotted in in Fig. 7b were computed from the averages of the off-diagonal terms of  $[\bar{\mathbf{C}}]$  in Eq. (4). To test the symmetry of  $[\bar{\mathbf{C}}]$ , we computed the off-diagonal differences  $\bar{C}_{12} - \bar{C}_{21}$ ,  $\bar{C}_{13} - \bar{C}_{31}$ , and  $\bar{C}_{23} - \bar{C}_{32}$  (recall that all nine components of  $[\bar{\mathbf{C}}]$  were found as a best-fit among over two hundred probes). The results are shown in Fig. 8, in which each difference has been normalized by dividing it by the corresponding off-diagonal average (for example, the difference  $\bar{C}_{12} - \bar{C}_{21}$  has been divided by  $\frac{1}{2}(\bar{C}_{12} + \bar{C}_{21})$ ). The results clearly reveal a significant asymmetry of the compliance matrix: the compliances  $\bar{C}_{12}$  and  $\bar{C}_{13}$  unmistakably differ from their counterparts, and the difference grows with increasing strain. Taking the naive approach of computing all nine compliances does result in some small inconsistencies, with small erratic differences  $\bar{C}_{23} - \bar{C}_{32}$  and tiny differences between  $\bar{C}_{12}$  and  $\bar{C}_{13}$  that are at variance with the presumed transverse isotropy. These inconsistencies are small and inconstant, however, and they are certainly insignificant when compared with the persistent asymmetry of the reversible compliance that grows with increasing strain. This result demonstrates that the reversible operator  $\mathcal{C}^{(r)}$  can not be strictly derived from a strain energy density function.



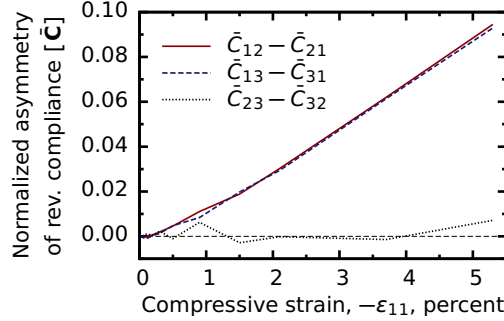


Figure 8: Asymmetry of the reversible compliance matrix  $[\bar{\mathbf{C}}]$ , expressed in the differences of its off-diagonal terms. The differences are normalized by dividing by the average values of the same off-diagonal terms.

## 5. Analysis of irreversible strains

We now consider the incremental irreversible behavior in relation to conventional elasto-plasticity and evaluate the consistency with (or divergence from) this constitutive framework. This analysis reveals new complexities in the irreversible response of granular materials. With conventional elasto-plasticity, the strain increment is the sum of reversible and irreversible parts, and in the previous section, we found that the reversible part,  $d\boldsymbol{\varepsilon}^{(r)}$  or  $d\boldsymbol{\varepsilon}^{(r)}$ , was a linear function of the stress increment: a compliance operator  $\mathbf{C}$  multiplied by the stress increment. Because the particles' contact mechanism is rate-independent, the bulk material behavior is also rate-independent and the functional relationship between the irreversible strain and the stress increment,  $d\boldsymbol{\varepsilon}^{(i)} = \mathbf{C}^{(i)}(d\boldsymbol{\sigma})$ , must be homogeneous of degree 1 with respect to the stress increment  $d\boldsymbol{\sigma}$ . The rate-independent constitutive function  $\mathbf{C}^{(i)}$  can depend upon the direction of the stress increment,  $d\boldsymbol{\sigma}/|d\boldsymbol{\sigma}|$ , as well as on its magnitude  $|d\boldsymbol{\sigma}|$  (see [48] and the proposition of tensorial zones in [49]). In conventional elasto-plasticity, the relationship  $\mathbf{C}^{(i)}$  is assumed to be incrementally bi-linear with two tensorial zones that are half-spaces separated by a hyper-plane (yield surface) having the unit normal  $\mathbf{f}$ . The irreversible strain increment of conventional elasto-plasticity is expressed as

$$[d\boldsymbol{\varepsilon}^{(i)}] = \begin{cases} 0, & [\mathbf{f}]^T [d\boldsymbol{s}] \leq 0 \\ \frac{1}{h} [\mathbf{g}] [\mathbf{f}]^T [d\boldsymbol{s}], & [\mathbf{f}]^T [d\boldsymbol{s}] > 0 \end{cases} \quad \text{or} \quad [d\boldsymbol{\varepsilon}^{(i)}] = \begin{cases} 0, & [\bar{\mathbf{f}}]^T [d\boldsymbol{\sigma}] \leq 0 \\ \frac{1}{\bar{h}} [\bar{\mathbf{g}}] [\bar{\mathbf{f}}]^T [d\boldsymbol{\sigma}], & [\bar{\mathbf{f}}]^T [d\boldsymbol{\sigma}] > 0 \end{cases} \quad (5)$$

for the alternative systems of generalized stress and strain vectors,  $[d\boldsymbol{s}]$  and  $[d\boldsymbol{\varepsilon}^{(i)}]$ , and of their Cartesian counterparts  $[d\boldsymbol{\sigma}]$  and  $[d\boldsymbol{\varepsilon}^{(i)}]$  (see Eqs. 1–3). In these expressions,  $[\mathbf{f}]$  is the unit vector of the yield direction;  $[\mathbf{g}]$  is the unit flow direction, which is the direction of the irreversible strain  $[d\boldsymbol{\varepsilon}^{(i)}]$ ; and  $h$  is the scalar plastic modulus. Over-bars are used to distinguish the Cartesian counterparts, noting that the two systems — generalized and Cartesian — are formed from triads of orthonormal basis vectors (Eq. 1), and one can readily shift between the two systems: with  $[\bar{\mathbf{f}}] = [\mathbf{f}] [\mathbf{E}]^T$ ,  $[\bar{\mathbf{g}}] = [\mathbf{E}] [\mathbf{g}]$ , and  $h = \bar{h}$ .

We now investigate this question: does the conventional plasticity of Eqs. (5) match the incremental behavior of the simulations? The question has four aspects, which correspond to the principles 3–6 of the Introduction: (3) whether a stress direction of purely elastic response exists; (4) whether a single yield surface with normal direction  $\mathbf{f}$  separates two tensorial half-spaces of irreversible and reversible behaviors; (5) whether irreversible strain is uniformly in a single

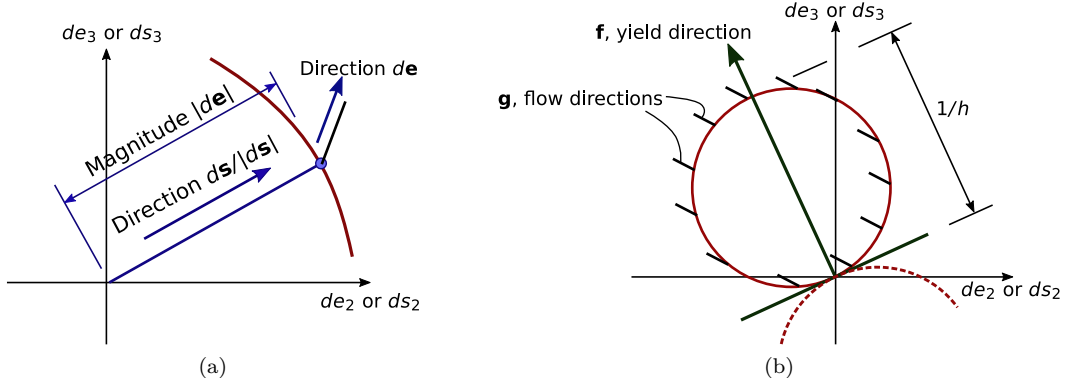


Figure 9: Plotting the irreversible stress–strain relationship with polar plots and spars (as in Eq. 6). The example shown is for behavior within the  $\bar{e}_2$ – $\bar{e}_3$  plane: (a) points represent magnitudes and directions of the irreversible strain; and (b) conformity with conventional elasto-plasticity creates a circular polar locus.

direction  $\mathbf{g}$  that is independent of the stress increment  $d\boldsymbol{\sigma}$ ; and (6) whether the irreversible strain  $d\mathbf{e}^{(i)}$  is proportional to the projected stress  $[\mathbf{f}]^T[d\boldsymbol{\sigma}]$ . Based upon the discussion of Fig. 3, one must suspect that the first question is answered in the negative, since we had found that irreversible deformation occurs during both compressive loading and extensional unloading, which suggests that a region of purely elastic behavior, if it exists at all, is smaller than the strain increment of  $2 \times 10^{-6}$  that was used in our simulations. Answers to the four questions, although somewhat hidden within Figs. 3–6, are clearly revealed in special polar plots of the simulation results.

Our plotting method is illustrated in Fig. 9 and is applied in Fig. 10, the latter showing results of the material’s response in three series of probes, with each probe sharing a common magnitude of the stress increment,  $|ds|$ . Figure 10 is for probes initiated at the compressive strain  $\varepsilon_{11} = 0.9\%$ , at which the deviatoric stress had advanced to 78% of the peak strength. The three series of probes were conducted in the three orthogonal planes: the Rendulic plane  $d\bar{e}_1$ – $d\bar{e}_3$ , the octahedral pi-plane  $d\bar{e}_2$ – $d\bar{e}_3$ , and the plane  $d\bar{e}_1$ – $d\bar{e}_2$  of volumetric and transverse-deviatoric increments. Because generalized stress and strain,  $[ds]$  and  $[de]$ , share the same basis vectors, the planes in Fig. 10 represent both stress and strain. Each sub-figure depicts two different aspects of behavior, as illustrated in Fig. 9a. The closed solid (red) line is a polar plot of the magnitude of the strain increment  $|de|$ , and it is directly related to the yield condition  $\mathbf{f}$ . The thin short spars show flow directions  $\mathbf{g}$ , and these spars are discussed further below. Each closed solid (red) line is the locus of points

$$\frac{|de^{(i)}|}{|ds|} \frac{ds}{|ds|} \longrightarrow \text{Figure 10 locus} \quad (6)$$

of the over eighty probes for one of the three series of probes. That is, the radial distance from the origin of a plot to a point on the solid curve is the magnitude of the irreversible strain increment  $|de^{(i)}|$  that results from a stress increment of magnitude  $|ds|$  (i.e. the first quotient in Eq. 6). The radial line is oriented in the *direction* of the stress increment,  $ds/|ds|$ , that produced the strain increment (this quotient is a unit vector in stress space, whereas the radial distance  $|de^{(i)}|$  is a scalar measure of the irreversible strain).

We now return to the conventional plasticity of Eq. (5): if the irreversible strain conforms to this equation, then the locus of points in Eq. (6) will be a sphere (Fig. 9b, noting that the lower sphere is disallowed by the condition  $[\mathbf{f}]^T[ds] > 0$  in Eq. 6). That is, if the conventional plasticity

of Eq. (5) holds, then the solid curves in the cross-sections of Fig. 10 should be circles, regardless of the plane that is being represented in the generalized space of  $ds^{(i)}$ . The generating sphere of these circles would pass through the origin, its radius would be  $1/h$ , and the tangent plane of the sphere at the origin would have the unit normal direction  $\mathbf{f}$ . These characteristics for a plot of Eq. (5) are independent of the flow direction  $\mathbf{g}$ . As such, we can test whether the material conforms to the ideal yield condition by observing the shapes of the solid curves in each of the planes of Fig. 10. Note that similar results would also apply to the space of Cartesian increments,  $[d\boldsymbol{\varepsilon}^{(i)}]$  and  $[d\boldsymbol{\sigma}]$ , as this system also has an orthonormal basis.

The plots in Figs. 9 and 10 also include a series of short thin spar lines that show the *directions* of the irreversible strain  $de^{(i)}$  for different directions of the stress increment,  $ds/|ds|$ , with the direction of  $de^{(i)}$  projected onto the plane of the plot. That is, the radial direction from the origin to a point on the closed curve is the stress direction  $ds/|ds|$ , the radial distance is the strain magnitude  $|de|/|ds|$ , and the spar shows the direction of the irreversible strain  $[de^{(i)}]/|de^{(i)}|$  that results from the stress increment (Fig. 9a, where the strain direction vector is projected onto each particular plane). Conformity with conventional elasto-plasticity (Eq. 5 and principle 5) demands a uniform direction and length of these spars.

Figure 10a shows these results for the Rendulic plane of volumetric and deviatoric stress and strain. The radial ruler in this plot gives the scale of strain magnitude,  $|de|$  or  $|d\boldsymbol{\varepsilon}|$ , for the closed curve. The closed curve is an almost perfect circle, meaning that the conventional plasticity of Eq. (5) does seem to apply for axisymmetric *triaxial* probes in which various combinations of mean stress  $dp$  and deviator stress  $dq$  are applied (i.e., probes in the Rendulic plane  $d\vec{s}_1-d\vec{s}_3$ ). The diameter of the circle in Fig. 10a is the inverse plastic modulus, such that  $h = 17.6$  MPa. The circle is tilted at angle  $\theta = 121^\circ$  from the  $d\vec{s}_1$  axis, with the unit yield vector  $\mathbf{f}$  would have direction  $[\cos \theta, 0, \sin \theta]^T$  in the generalized stress-space  $[ds]$ . This yield direction considers only behavior within the Rendulic plane, whereas the out-of-plane behavior is considered below. The yield direction  $\mathbf{f}$  corresponds to a yield “friction angle”  $\sin^{-1}((d\sigma_{11} - d\sigma_{33})/(d\sigma_{11} + d\sigma_{33})) = 33^\circ$  for these triaxial conditions. At the stage of loading of the figure, the mobilized friction angle  $\sin^{-1}((\sigma_{11} - \sigma_{33})/(\sigma_{11} + \sigma_{33}))$  was  $30^\circ$ , somewhat less than the yield angle.

Upon close inspection, however, a second but much smaller circle is also present in the Rendulic plane, below and to the right of the larger circle. A detail of this circle is shown in Fig. 10d, demonstrating that a small amount of dissipative, irreversible strain occurs during a reversal of triaxial compression. The two circles, forward and reverse (loading and unloading), are nearly (but not quite) tangent to each other and to the same oblique line in the Rendulic plane that defines the perpendicular angle  $\theta$ . As with the generalized plasticity model of Zienkiewicz and Pastor [30], irreversible deformation is activated for opposite directions of the stress increment — for both loading and unloading — with yield directions  $\mathbf{f}_{\text{loading}} = -\mathbf{f}_{\text{unloading}}$ . In regard to the conventional plasticity of Eq. (5), the irreversible strain increment for the first, “elastic” case is not zero, but instead has a form similar to that of the second, “plastic” case, but with a much larger modulus  $h$  (the plastic moduli for loading and unloading are 17.6 MPa and 720 MPa, respectively). In Fig. 10d, we also note that the two circles, large and small, do not exactly meet at a common point, demonstrating that irreversible strain occurs in all  $360^\circ$  of loading within the Rendulic plane, thus abrogating principle 3 of a finite elastic domain within the axisymmetric Rendulic plane. This result, which can only be discerned by applying very small strain increments, was not reported in past studies. The absence of a loading direction that produces purely reversible strain is shown also to apply in the two other planes of loading.

Returning to the Rendulic plane of Fig. 10a and ignoring for the moment the small unloading circle at the bottom right of this figure, the spars are almost uniformly aligned in the same direction

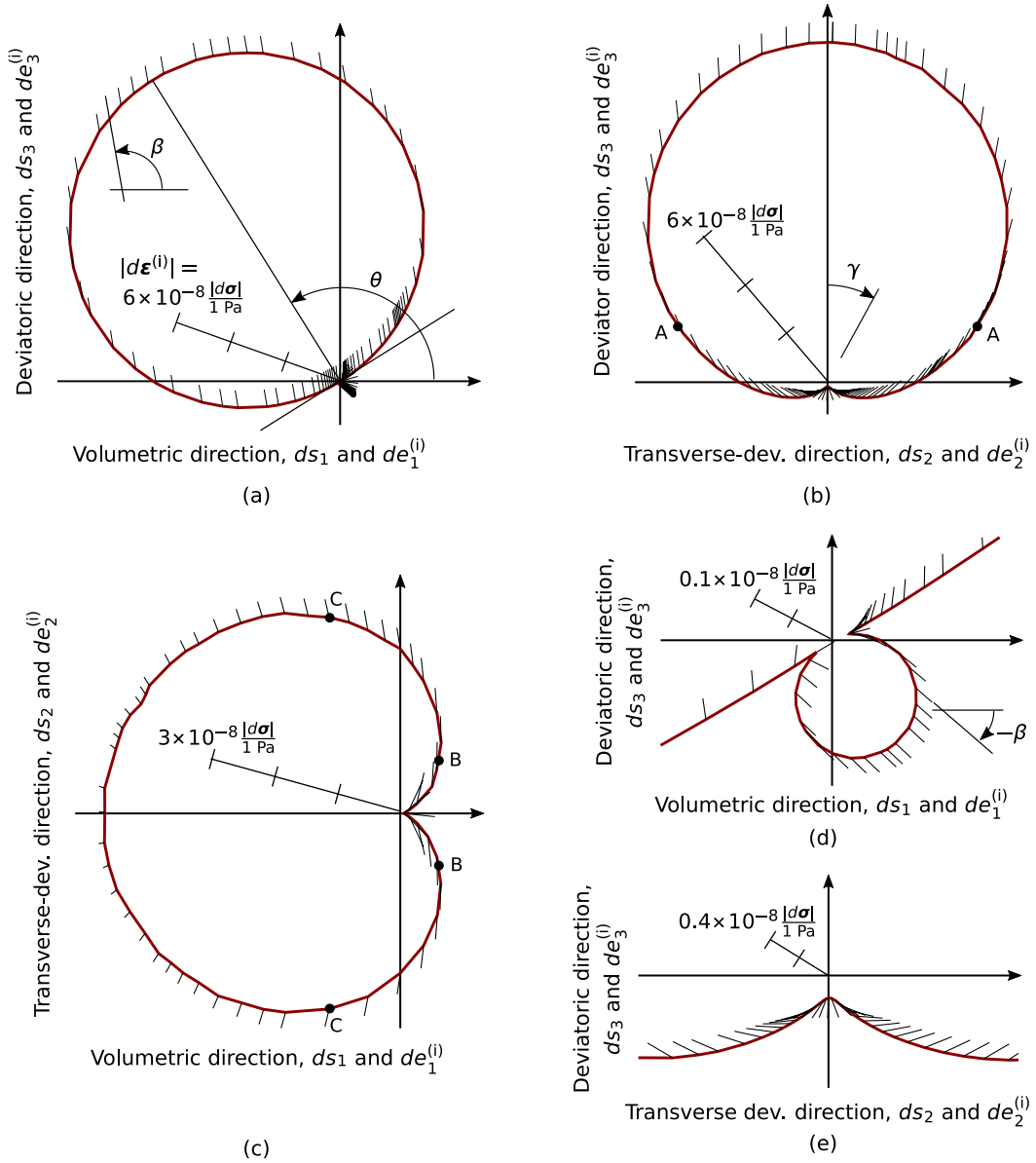


Figure 10: Polar plots showing the results of multiple probes in the the generalized space of irreversible strain  $d\bar{\epsilon}^{(i)}$  and of stress  $d\bar{\sigma}$ . As with Eq. (6), radial distance from the origin represents the irreversible strain magnitude  $|d\epsilon^{(i)}|$  produced by a stress increment of the corresponding direction  $ds/|ds|$ . Short spars show the directions of the irreversible strains: (a) Rendulic plane of volumetric and deviatoric increments, (b) pi-plane of deviatoric and transverse-deviatoric increments, (c) plane of volumetric and transverse-deviatoric increments, (d) detail of the Rendulic plane, and (e) detail of the pi-plane. The probes are at a reference strain  $\epsilon_{11} = -0.9\%$  and were conducted with Cattaneo–Mindlin contacts.

around the larger circle, regardless of position on the circle (i.e., regardless of the direction of the stress increment). Although an important exception will be noted below, this result means that a single flow direction  $\mathbf{g}$  applies to axisymmetric triaxial loading within the Rendulic plane (see Eqs. 5). A similar uniformity of flow direction in the Rendulic plane of axisymmetric loading has also been found in 2D simulations [11], in 3D simulations [14, 20, 21], and in soil experiments [9, 10, 12, 47]. The conclusion of a nearly uniform direction in the Rendulic plane would also be suspected from the results in Figs. 4d and 5b: the curves of irreversible strain  $d\mathbf{e}^{(i)}$  appear as straight lines in these views, confirming a nearly uniform direction of  $d\mathbf{e}^{(i)}$  in the  $d\vec{\mathbf{e}}_1$ – $d\vec{\mathbf{e}}_3$  plane. This observation is somewhat deceptive, however, as a full plane of fanned flow directions might appear as a line in the edge-wise perspective of these figures, as will be demonstrated below.

The flow spars around the larger circle in Fig. 10a are oriented upward and to the left, at an angle of  $\beta = 100^\circ$  relative to the  $d\vec{\mathbf{e}}_1$  direction of purely isotropic compression, indicating that the incremental irreversible strain is dilative. This orientation corresponds to a dilatancy angle  $\psi^{(i)} = \sin^{-1}((d\varepsilon_{11}^{(i)} + d\varepsilon_{33}^{(i)})/(d\varepsilon_{11}^{(i)} - d\varepsilon_{33}^{(i)}))$  of  $10^\circ$  and an irreversible dilation rate  $dv^{(i)}/|d\varepsilon_{11}^{(i)}|$  of 0.43. As with most studies listed in Table 1, the orientations of yield and flow,  $\mathbf{f}$  and  $\mathbf{g}$ , do not coincide, with  $\beta \neq \theta$ , and the irreversible response is clearly non-associative.

For the small circle that corresponds to triaxial unloading (Fig. 10d), the irreversible strain direction is almost uniformly downward and to the right with an angle  $\beta = -45^\circ$ , such that unloading increments produce irreversible volume compression rather than dilation. Figure 10d shows that irreversible strain occurs in two different directions for triaxial (Rendulic) loading and unloading, with  $\mathbf{g}_{\text{loading}} \neq \mathbf{g}_{\text{unloading}}$ . Similarly, the results of Lewin and Burland [9] and Tatsuoka and Ishihara [10] also indicated a difference in the directions of plastic strain for stress increments that produce loading and those that produce unloading, a difference that is accommodated with generalized plasticity [50, 30].

A seemingly abrupt, discontinuous change in the direction of the irreversible strain (the directions of the spars) occurs at the two cusps in Fig. 10d, suggesting that the direction of the strain increment might be indeterminate when the stress increment is tangential to the yield direction (directions  $\theta = 121^\circ \pm 90^\circ$  in Fig. 10a). This result is troubling, as it suggests a violation of Hashiguchi’s continuity requirement [51], which holds that the total strain increment is identical for infinitesimally close loading directions (e.g., for directions on either side of the cusp in Fig. 10d). To evaluate continuity, we conducted more finely spaced probes at these and at other cusps, which will be discussed below.

Note, too, that purely volumetric loading — increments  $ds$  along the horizontal axis in Fig. 10d — produces irreversible increments of both volumetric and deviatoric strain. For an increasing pressure (toward the right of the origin in Fig. 10d), the volume change, although small, is finite, such that the irreversible reduction of volume  $dv^{(i)}$  is equal to  $dp/2.1$  GPa. This observation is consistent with soil behavior that is described with “capped” yield surfaces that activate plastic deformation with increasing pressure increments [52] (note, however, that no such cap is invoked in the current work). The volumetric response is much softer for pressure reductions (toward the left of the origin in Fig. 10d), with  $dv^{(i)} = dp/16$  MPa. Cap models typically apply only to volumetric loading (compression), but the results in Fig. 10d show that both deviatoric and volumetric irreversible strains are induced by both volumetric and deviatoric unloading (downward and to the left in Fig. 10d), a result that has not been revealed in previous studies.

We now turn attention to Fig. 10b, which displays results of the series of isobaric stress probes in the  $d\vec{\mathbf{s}}_2$ – $d\vec{\mathbf{s}}_3$  octahedral pi-plane of deviatoric loading (i.e., similar to the results displayed in Fig. 5b). In a laboratory setting, such stress increments could be produced with true-triaxial

equipment. The closed solid curve in this figure was produced in the manner of Eq. (6). The curve is clearly not a circle passing through the origin, meaning that the ideal conventional plasticity of Eqs. (5) does not apply to true-triaxial deviatoric or to transverse-deviatoric loadings. For example, the curve's breadth (in the  $ds_2$  direction) is greater than its height above the  $ds_3$  axis, indicating softer behavior in the transverse direction. The curve also passes *below* the horizontal axis, which means that deviatoric unloading (with  $ds_3$  or  $dq \leq 0$ ) produces irreversible strain.

If one assumes that a single yield direction  $\mathbf{f}$  applies and that the yield surface is a plane of orientation  $\theta$  and is perpendicular to the Rendulic plane of Fig. 10a, then the transverse-deviatoric  $\vec{s}_2$  direction is tangent to the yield surface. The fact that irreversible deformation occurs in these tangential loading directions ( $ds_3 \leq 0$  and  $de_2^{(i)} \neq 0$ , or the 3 o'clock to 9 o'clock directions in Fig. 10b) confirms the long-held conjecture of tangential plasticity. Evidence of tangential plasticity has also been revealed in the 3D simulations of Kishino [14] and Plassiard et al. [20]. The conjecture of tangential plasticity originated from Hill's analysis of multi-slip crystal plasticity [31] and as a possible rationale for softer behavior in loading directions that could produce certain localized modes of deformation [53, 4], and a simple two-mechanism model is investigated in Section 6.1. Similar to multi-slip plasticity models, certain micro-mechanics models of granular materials are based upon presumed distributions of contact orientations and upon the normal and tangential interactions on contact planes of different orientation [54, 55, 56]. These hypothetical models also lead to tangential plasticity, although they presume a single, averaged behavior to all contacts with the same orientation, assume affine movements among the particles, and homogenize movements across the space of orientations. Recent DEM simulations have shown, however, that micro-scale movements are irregular and non-affine, with particles seemingly darting and dodging in a highly irregular manner, and that contact movements are highly diverse, even when one considers a subset of contacts having the same orientation [57, 58, 59]. Moreover, a fraction of contacts are persistently non-elastic and continue to undergo frictional slip even when the direction of bulk deformation is reversed [24].

The solid line in Figs. 10b and 10e is also concave near (and below) the origin of the figure. When plotted in the manner of Eq. (6), the behavior is clearly incompatible with conventional elasto-plasticity: the yield condition (yield surface) is seemingly cornered; a single yield direction  $\mathbf{f}$  does not apply; and transverse-deviatoric increments  $ds_2$  and deviatoric unloading  $ds_3 < 0$  generate irreversible strains, a result not revealed in previous experiments or simulations. A blunt corner *below the origin* is present in the detail of Fig. 10e, a result that has not been recognized in previous experiments and simulations. In their micro-fissure model for rock, Rudnicki and Rice [53] showed that a cornered elastic regime is associated with a reduced stiffness in the transverse direction, due to the irreversible strains that would accompany transverse loading (note, too, that the *reversible* stiffness is also reduced in the transverse direction, as seen in Fig. 7a). Unlike their micro-fissure model, however, an elastic regime does not exist in the  $\vec{s}_2$ – $\vec{s}_3$  plane, as the closed curve in Figs. 10b and 10e fully encloses the origin, demonstrating that irreversible deformation occurs in all loading directions within the pi-plane.

Figures 10b and 10e also depict the *directions* of irreversible strain,  $d\epsilon^{(i)}$  or  $d\mathbf{e}^{(i)}$ , as the short spars that emanate from the closed curve. Each spar begins from a point on the curve that corresponds to the direction  $ds$  of the applied stress increment. The results clearly show that irreversible deformation is not aligned in a uniform direction for different directions of loading,  $[ds]/|ds|$ . As one moves from the top of the closed curve, around the sides, and toward the bottom, the direction of the irreversible strain progressively points further away from the upward  $d\vec{e}_3$  direction. Therefore, a single flow direction  $\mathbf{g}$  (as in Eq. 5) does not apply to loading within the deviatoric pi-plane; instead, the flow direction is a function of the direction of the stress increment.

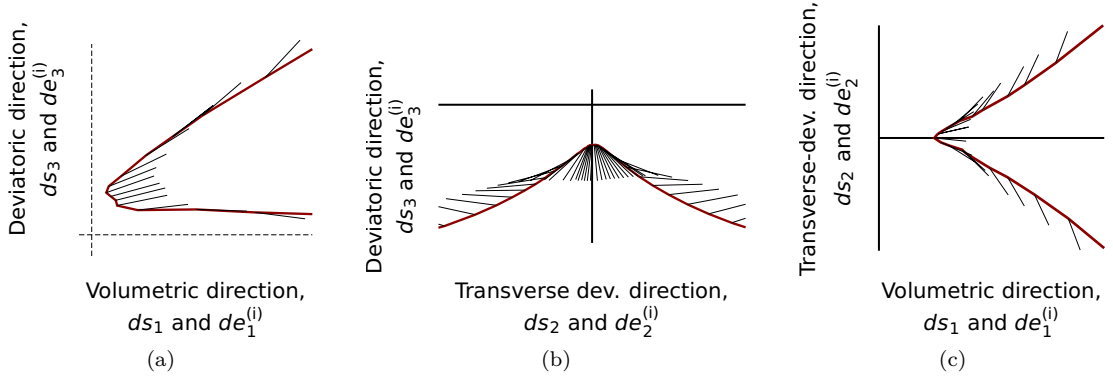


Figure 11: Magnified results at cusps: (a) cusp within the Rendulic plane, as in Figs. 10a and 10d; (b) cusp within the deviatoric plane, as in Figs. 10b and 10e; and (c) cusp within transverse-deviatoric–volumetric plane, as in Fig. 10c.

This result, which contradicts principle 5, has also been reported in previous simulations (see [14, 18, 23]). Moreover, irreversible strain can occur in any direction within the pi-plane — a full  $360^\circ$  of directions — if the proper stress direction  $ds/|ds|$  is applied. The transverse-deviatoric strain  $de_2^{(i)}$  is zero at the top and bottom of Fig. 10b (consistent with the initial axial symmetry), but  $de_2^{(i)}$  is largest at points “A” rather than in the  $\bar{s}_2$  direction along the horizontal axis.

The spars in Fig. 10b show projections of irreversible strain onto the isobaric pi-plane, but volume change is also induced by deviatoric loading. For the upper two quadrants of the figure (positive deviator stress  $q$ ), the irreversible volumetric strain  $de_1^{(i)}$  is dilative, but the direction is reversed in the lower half of the diagram, and the irreversible volume change is compressive for the entire portion of the pi-plane shown in Fig. 10e. Such observations are inconsistent with the conventional elasto-plasticity of Eq. (5) and have not been previously reported.

The situation is also complex when we consider loading increments within the transverse plane  $d\bar{e}_1-d\bar{e}_2$ , shown in Fig. 10c and unique to the current study. The horizontal axis of this plot represents increments of volume (or pressure), with compression to the right, and the vertical axis corresponds to deviatoric loading,  $ds_2$  or  $de_2$ , that is *transverse* to the axisymmetric triaxial deviator (i.e., transverse to  $ds_3$  and  $de_3$  in Eq. 1). The deviatoric stress increment,  $ds_3^{(i)}$  or  $dq$ , is zero within this plane. For loading within this  $d\bar{e}_1-d\bar{e}_2$  plane, the yield condition is bluntly cornered, irreversible flow varies with the direction of the stress increment  $ds/|ds|$  (i.e., incremental nonlinearity), and irreversible strain occurs with all directions of loading. Dilation occurs for most loading directions, but compression (contraction) occurs for directions between the points “B”. The transverse-deviatoric strain  $de_2^{(i)}$  is largest at points “C”. Irreversible flow, represented by the short spar lines, can occur in a wide swath of directions — a full  $360^\circ$  of directions — within the plane, depending upon the loading direction  $ds/|ds|$ .

Seeming cusps appear in all of the loading planes of Fig. 10. In a final set of these special plots, Fig. 11 magnifies the results at these locations. In each case, we see that the direction of irreversible strain (the spars in this figure) does not change abruptly, which would have indicated a discontinuity in the response and a violation of the Hashiguchi continuity requirement described above [51]. The solid lines are not pointed but are rounded, and as one traces along any of the solid lines in the figure, the directions of the spars (i.e., the directions of the irreversible strain) change rapidly but in a continuous manner.

Considering all of the plots in Fig. 10, none of the closed curves showing the irreversible

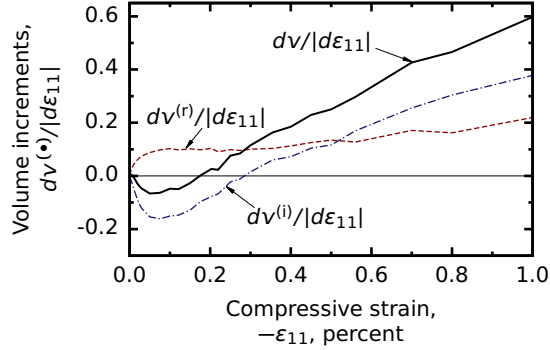


Figure 12: Contributions of reversible and irreversible strains to the rate of volume change during constant- $p$  triaxial compression.

response passes through the origin of the  $d\vec{e}_1-d\vec{e}_2-d\vec{e}_3$  system. In contravention of conventional elasto-plasticity (principle 3) and of more general models that are based on neutral loading directions [60], we can conclude that a reversible (elastic) regime, if it exists at all, is smaller than the strain increments of  $2 \times 10^{-6}$  that were used in these simulations. This characteristic has been suggested by Royis and Doanh [13] on the basis of their tests on sands that employed much larger strain increments. Alonso-Marroquín and Herrmann [15] also arrived at this conclusion by unloading a DEM assembly of polygons and then reloading on various paths. Many of our results, however, have not been observed in the previous studies listed Tables 1–3: including the irreversible strains that occur during reversed loading in the Rendulic plane, the directions of the transverse-deviatoric (tangential) strain increments, the cornered nature of yield within the pi-plane, etc. Had we solely relied on Gudehus response envelopes, such as those in Figs. 3c and 4d, these phenomena would have been missed in the current study, and they were only recognized by plotting data in a special manner of Figs. 9 and 10.

As a final observation, Fig. 12 shows the contributions of the reversible and irreversible strains to the rate of volume change  $dv/|d\varepsilon_{11}|$ . For our loading with initial loading with constant mean stress (constant- $p$ ), the total rate of volume change  $dv$  was negative (contractive) at the start of loading but transitioned to a positive (dilatant) rate at a strain of 0.2% (i.e., the “characteristic state” of soil behavior). As concluded in Section 4, the contribution of the reversible strain  $dv^{(r)}$  was dilatant throughout the loading, due to the anisotropy that was induced in the stiffness moduli. The irreversible volume change  $dv^{(i)}$  transitions from contractive to dilatant and becomes the dominant influence on volume behavior at strains beyond 0.5%.

## 6. Advanced models

Among other unusual aspects of our results, the shapes in Figs. 10b–10e demonstrate that behavior is softer in the transverse-deviatoric direction  $d\vec{s}_2$  than would be predicted by the conventional plasticity of Eq. (5). Several advanced theories of incremental stiffness have been proposed for modeling such behavior (see summaries by Bardet [11] and Hashiguchi et al. [4]), and we considered two modest enhancements of the conventional elasto-plasticity of Eq. (5): the multi-mechanism model of Mandel [31, 61] and the tangential plasticity model of Rudnicki and Rice [53]. For reasons that are described later, the most promising approach is a multi-mechanism model, which we now describe in the context of the simulation results.



### 6.1. Multi-mechanism model

The corners in Figs. 10 and 11, although rounded, suggest an incrementally multi-linear form of the yield condition (yield surface), rather than the single-mechanism assumption of conventional plasticity in Eq. (5). Our simulations were of multi-directional increments after an initial stage of axisymmetric triaxial loading. For this special case of initial loading, we would expect that the multiple mechanisms are symmetric with respect to the plane of loading — the  $d\vec{s}_1$ – $d\vec{s}_3$  Rendulic plane — and we consider two mechanisms, with yield directions  $\mathbf{f}_1$  and  $\mathbf{f}_2$  that are mirrored with respect to this plane. Although it is possible for the two types of yielding to produce flow  $\mathbf{g}$  in the same direction, the symmetric fanning of the irreversible spars in Figs. 10b and 10c suggests that the two mechanisms produce flow in directions that are also symmetric with respect to the  $d\vec{s}_1$ – $d\vec{s}_3$  plane. When both mechanisms are activated, the direction of irreversible strain can have a component in the transverse  $d\vec{e}_2$  direction, and the magnitude of this transverse component will depend upon the unbalanced activation of the two mechanisms. Moreover, the large and small circles in the Rendulic planes of Figs. 10a and 10d indicate that each of the two mechanisms will produce irreversible strains for both loading and unloading increments of stress. In this respect, we diverge from the multi-mechanism model of Mandel [62], who hypothesized distinctly reversible and irreversible tensorial zones with a specific flow direction for each mechanism.

Considering these observations, the DEM trends are consistent with a two-mechanism model for the irreversible strains of the form

$$d\mathbf{e}^{(i)} = d\mathbf{e}_1^{(i)} + d\mathbf{e}_2^{(i)} = \mathcal{F}_1^{(i)}(d\mathbf{s}) + \mathcal{F}_2^{(i)}(d\mathbf{s}) \quad (7)$$

$$\mathcal{F}_a^{(i)}(d\mathbf{s}) = [d\mathbf{e}_a^{(i)}] = \begin{cases} \frac{1}{h^-} [\mathbf{g}_a^-] [\mathbf{f}_a]^T [d\mathbf{s}], & [\mathbf{f}_a]^T [d\mathbf{s}] \leq 0 \\ \frac{1}{h^+} [\mathbf{g}_a^+] [\mathbf{f}_a]^T [d\mathbf{s}], & [\mathbf{f}_a]^T [d\mathbf{s}] > 0 \end{cases}, \quad a = 1, 2 \quad (8)$$

with the subscript,  $a = 1$  or  $2$ , denoting the particular mechanism. Each mechanism has different plastic moduli,  $h^+$  and  $h^-$ , in the loading and unloading directions, as suggested by generalized plasticity models [53, 4]. Because of the axial symmetry of the initial triaxial loading, the two unit yield directions,  $\mathbf{f}_1$  and  $\mathbf{f}_2$ , activate mechanisms that are symmetric with respect to the  $d\vec{s}_1$ – $d\vec{s}_3$  plane: the two directions share the same orientation in the  $d\vec{s}_1$ – $d\vec{s}_3$  plane (such as the angle  $\theta$  in Fig. 10a) but have mirrored directions that tilt out-of-plane (i.e., the directions  $\mathbf{f}_1$  and  $\mathbf{f}_2$  are rotated by angles  $\gamma$  and  $-\gamma$  about the  $d\vec{s}_1$  axis, Fig. 10b). Different unit flow directions,  $\mathbf{g}^+$  and  $\mathbf{g}^-$ , apply to loading and unloading, as is apparent from the spars that emanate from the large and small circles of Fig. 10d. The flow directions are in pairs,  $(\mathbf{g}_1^+, \mathbf{g}_2^+)$  and  $(\mathbf{g}_1^-, \mathbf{g}_2^-)$ , with each pair mirrored with respect to the  $d\vec{s}_1$ – $d\vec{s}_3$  plane, with orientation angles  $\beta_1^+ = \beta_2^+$  and  $\beta_1^- = \beta_2^-$  in the  $d\vec{s}_1$ – $d\vec{s}_3$  plane (Fig. 10a), and tilted about the  $d\vec{s}_1$  axis at the same angles  $\gamma_1 = -\gamma_2$  as are the yield directions (Fig. 10b). In the spaces of the generalized stress and strain of Section 3.1, the yield direction  $\mathbf{f}_a = [\cos \theta_a, \sin \theta_a \sin \gamma_a, \sin \theta_a \cos \gamma_a]^T$ ; and the flow direction  $\mathbf{g}_a^\pm = [\cos \beta_a^\pm, \sin \beta_a^\pm \sin \gamma_a, \sin \beta_a^\pm \cos \gamma_a]^T$ .

This generalized two-mechanism model that includes irreversible unloading reasonably fits the simulation data (Fig. 13). It's four tensorial zones are subtly apparent as the circular lobes of the dashed blue lines of Figs. 13b and 13c. The two mechanisms combine to create the features of irreversible deformation that were found with the DEM simulations: for example, at the strain  $\varepsilon_{11} = -0.9\%$  of Fig. 10, a yield angle  $\theta = 121^\circ$  with respect to the isotropic axis, a dilation direction  $\beta = 100^\circ$  with respect to this axis, cusped corners, a vanishing elastic region, irreversible volumetric yielding, and the dependence of the flow direction on the direction of

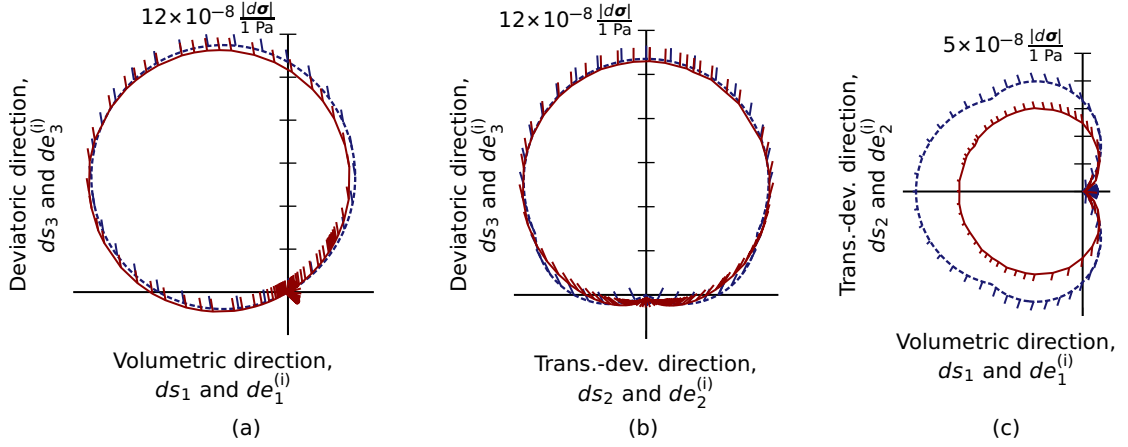


Figure 13: Comparison of DEM probes with the two-mechanism model of Eqs. (7) and (8), at strain  $\varepsilon = -0.3\%$ . Plots correspond to those in Figs. 10a, 10b, and 10c. Dashed lines (blue) are predictions of the two-mechanism model, with the best-fit parameters given in Table 4. Solid red lines are the simulation result of Fig. 10. The vertical rule and scale indicate the inelastic strain magnitude  $|d\varepsilon|$ .

Table 4: Best-fit parameters for the two-mechanism model of Eqs.(7) and (8) for the simulation results with Cattaneo-Mindlin contacts. Model results are shown in Fig. 13.

Strain	Hardening		Yield direction, $\mathbf{f}$		Flow direction, $\mathbf{g}$	
	$h^+$	$h^-$	$\theta_1 = \theta_2$	$\gamma_1 = -\gamma_2$	$\beta_1^+ = \beta_2^+$	$\beta_1^- = \beta_2^-$
0.3%	11.2 MPa	1,650 MPa	113°	25°	90.2°	-41°
0.9%	6.6 MPa	830 MPa	119°	26°	99.4°	-41°
5.3%	4.4 MPa	360 MPa	128°	26°	117.5°	-37°

the stress increment. The best-fit parameters of the two-mechanism model are summarized in Table 4 for loading probes at the strains 0.3%, 0.9%, and 5.3%. The fit in Fig. 13 is certainly not perfect, with an average mismatch in the strains  $de^{(i)}$  that is 14% of the average magnitude  $|de^{(i)}|$ . Figure 13c shows that this error originates primarily in the model's overestimation of the deviatoric strains  $de_3^{(i)}$  when the deviatoric stress  $ds_3$  is close to zero. The model also introduces subtle new corners that were not observed in the simulations: the slight corners seen in the second and third quadrants of Fig. 13c.

## 6.2. Tangential plasticity model

The alternative tangential plasticity model of Rudnicki and Rice [53] has a primary yield direction, say  $\mathbf{f}$ , but additional irreversible deformation is induced by tangential stress increments that are orthogonal to this direction. In the context of our results for an axisymmetric initial loading, direction  $\mathbf{f}$  lies in the  $\vec{s}_1$ - $\vec{s}_3$  Rendulic plane (for example, for the results at strain  $\varepsilon_{11} = -0.9\%$  of Fig. 10a,  $\mathbf{f}$  is directed at angle  $\theta = 121^\circ$ ), and the tangential direction is the transverse-deviatoric direction  $\vec{s}_2$ . A fairly general form for the additional deformation produced by tangential loading would be as follows: the sum of a tangential flow increment that is symmetric in the unit  $\vec{s}_2$  direction,  $(1/h_1)\vec{s}_2(\vec{s}_2 \cdot d\mathbf{s})$ , and a second flow increment that is anti-symmetric,  $(1/h_2)\mathbf{g}_2|\vec{s}_2 \cdot d\mathbf{s}|$ ,

where unit flow direction  $\mathbf{g}_2$  lies in the  $\vec{s}_1$ - $\vec{s}_3$  plane. Both of these irreversible flows are induced by loading in the transverse  $\vec{s}_2$  direction (i.e. from the projected stress increment  $\vec{s}_2 \cdot ds$ ). The anti-symmetric term in this model introduces an additional yield direction besides the primary direction  $\mathbf{f}$ , and as such, is a multi-mechanism model that also includes a symmetric (and linear) flow term, similar to the linear part of hypo-plastic models. Like the two-mechanism model described above, the tangential model includes additional tensorial zones and introduces two additional parameters. Despite its complexity, we found the fit to be less favorable than the simple two-mechanism model, and the average mismatch in the irreversible strains  $d\epsilon^{(i)}$  was 17% of the average strain magnitude  $|d\epsilon^{(i)}|$ .

## 7. Conclusions

The simulations reveal several fundamental aspects of incremental granular behavior, some of which deviate substantially from conventional elasto-plasticity and have not been reported in previous studies:

1. The reversible response that is produced by the initial axisymmetric triaxial loading conforms to an anisotropic linear model with transverse isotropy, with an exception noted below. The initial monotonic loading induced progressively more anisotropic reversible (elastic) stiffness with increased loading. Although this result is not surprising, the measured anisotropy was quite large, with the axial Young's modulus becoming as much as 6 times greater than the modulus in lateral directions. The anisotropy of the reversible stiffness, which increases with increasing strain, is consistent with the observed volumetric behavior of sands: the reversible strain, by itself, would transition from contractive to dilative under constant lateral stress or would transition from neutral to dilative under constant- $p$  loading.
2. Although the reversible (elastic) stiffness operator is symmetric at the start of loading, the incremental stiffness soon becomes asymmetric, with an asymmetry that grows as loading proceeds. The elastic compliance  $\bar{C}_{ij}$  becomes greater than  $\bar{C}_{ji}$  when “ $i$ ” and “ $j$ ” are the loading and transverse directions.
3. Irreversible strain occurs for all directions of the stress increment (loading, unloading, transverse-loading, etc.), and, as has been stated, a reversible domain, if it exists at all, is smaller than the very small strain increments of our simulations,  $2 \times 10^{-6}$ . In particular, a small irreversible strain even occurs when the initial axisymmetric triaxial loading is reversed (from triaxial compression to triaxial extension). That is, irreversible strains occur for all directions of stress increments within the  $p$ - $q$  Rendulic plane, abrogating the conventional concept of opposite loading (yield) and unloading (elastic) directions. Moreover, the irreversible strain during a reversed increment of triaxial extension is contractive, even as the irreversible strain is dilative during triaxial compression.
4. Following an initial loading along a path of axisymmetric triaxial compression, irreversible strains occur for stress increments in the transverse-deviatoric direction, and the deformation has isotropic, deviatoric, and transverse-deviatoric components. This transverse-deviatoric direction is tangent to the primary yield surface that would develop during the initial axisymmetric loading, and the observed irreversible strains are direct evidence of the tangential plasticity that was theorized by Rudnicki and Rice [53] and Hashiguchi [4]. Large irreversible strain increments occur in this transverse-deviatoric (tangential) direction

for a wide range of stress increment directions, and these irreversible increments have both volumetric and deviatoric components.

5. In the three planes formed by the axes of volumetric, deviatoric, and transverse-deviatoric stress, the yield surface displays rounded corners. Because the corners are rounded and not abrupt, the irreversible strains change in a continuous manner as the stress increment is varied near a corner.
6. The direction of the irreversible strain increment depends upon the direction of the stress increment: a single flow direction does not apply with granular materials. For stress increments within the octahedral pi-plane, the irreversible strain increments range from contractive to dilative for different stress directions.
7. During the initial monotonic constant- $p$  triaxial compression in which the mean stress was kept constant, the volume change in our simulations of a medium-dense sand was initially contractive but transitioned to dilative at larger strains (the transition from contractive to dilative behavior, referred to as the characteristic state, occurred at a strain  $\varepsilon_{11} = 0.1\%$ ). Under constant- $p$  conditions, these volume tendencies are the combined result of reversible and irreversible strain increments. The intense anisotropy that is developed in the reversible stiffness produces dilation throughout the loading process; whereas, the irreversible response was contractive at small strains but transitioned to dilative at larger strains. The strong dilation at large strains is produced by both reversible and irreversible responses.
8. The irreversible strains that were measured with DEM stress probes reasonably conform to a two-mechanism elasto-plasticity model, although the fit is not perfect. The yield and flow directions of each mechanism must have a component in the transverse-deviatoric direction that can produce the tangential irreversible strains that were measured with the simulations. The model must also include irreversible deformations in both loading and unloading directions. Our attempt to fit a more complex tangential plasticity model was less successful, due to the complex coupling of the three components of the irreversible strains.

Taken together, the results contradict five of the six principles of conventional elasto-plasticity that were given in the Introduction, and the results go further, by also revealing details of this contravening behavior.

We note that these results were derived from simulations with an assembly having Cattaneo–Mindlin contacts, which permit elastic, micro-slip, and slip behaviors at the contact level. The authors conducted similar simulations with conventional linear-frictional contacts, and all aspects of the results enumerated above were qualitatively the same as those with Cattaneo–Mindlin contacts.

Our study was limited to behavior that followed an initial monotonic drained triaxial compression, and this work could certainly be extended to more general loading paths: other proportional loading paths, paths involving principal stress rotations, and cyclic paths. The results suggest, however, that granular behavior is more complex than previously thought and that granular materials should be treated as thoroughly inelastic and anisotropic materials that can only be modeled, even approximately, with more advanced constitutive frameworks than conventional elasto-plasticity.

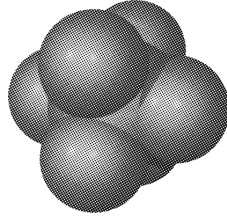


Figure A.14: Sphere-cluster particle.

## Appendix A. DEM modeling details and verification

Discrete element simulations were conducted with a cubical assembly of 10,648 particles contained within periodic boundaries. The primary DEM algorithm is that of Cundall and Strack [63], in which servo-controlled boundaries were used to maintain a constant mean stress during the initial monotonic loading and selective combinations of the principal stresses during stress probes [64, 65]. The simulations were intended to produce a modest fidelity to the bulk behavior of sands at low mean stress. Because sphere assemblies produce unrealistic rolling between particles and have a low bulk strength, we used a bumpy, non-convex cluster shape for the particles: a large central sphere with six smaller embedded outer spheres in an octahedral arrangement (Fig. A.14). The use of non-spherical particles circumvents the need of artificial measures to restrain the particle rotation [66, 67] (circumventing, for example, the use of rotational contact springs or the direct restraint of particle rotations, as in [20]). Through trial and error, we chose the radii of the central and outer spheres so that the bulk behavior approximated that of Nevada Sand, a standard poorly graded sand (SP) use in laboratory and centrifuge testing programs [68, 36]. The particle size range was 0.074–0.28 mm, with  $D_{50} = 0.165$  mm, with a size distribution that closely matched that of Nevada Sand.

To create assemblies with a range of densities, we began with the particles sparsely and randomly arranged within a cubic periodic cell. With an initial low interparticle friction coefficient ( $\mu = 0.20$ ), the assembly was isotropically reduced in dimension until it “seized” when a sufficiently complete contact network had formed. A series of 25 progressively denser assemblies were created by repeatedly assigning random velocities to the particles of the previous assembly and then further reducing the cell’s dimensions until it, too, had seized. The 25 assemblies had void ratios ranging from 0.781 to 0.586 (solid fractions of 0.561 to 0.664). The single assembly used in the paper had void ratio 0.690 (solid fraction 0.592) and approximates the behavior of Nevada Sand at a relative density of 40%. After compaction, the assembly was allowed to quiesce with friction coefficient  $\mu = 0.40$ , which was then raised to  $\mu = 0.55$  for the subsequent loading simulations (a value that produced drained and undrained behaviors similar to Nevada Sand [36]).

The particles are durable (non-breaking) and interact only at their contacts. Normal forces were modeled with a generalization of Hertz theory [69], and tangential forces were modeled with a full implementation of the complementary Cattaneo–Mindlin contact. The modified Hertz contact has the advantage of producing a small-strain shear modulus that is pressure-dependent, with a small-strain shear modulus that is proportional to pressure  $p$  raised to power 0.5, as is commonly observed in laboratory and field testing of sands [36]. With regard to tangential contact forces, approximate implementations of the Hertz contact typically use a tangential stiffness that is proportional to the normal force and not upon the directions of the normal and tangential movements [70, 71]. Such implementations do not permit frictional dissipation in the form of

micro-slip and can result in an unfortunate and physically inadmissible infusion of energy during close cycles of contact movement [40]. To avoid these problems, we used the Jäger algorithm for the tangential force, which can model arbitrary sequences of normal and tangential contact movements [39]. With the Cattaneo–Mindlin contacts, the loading simulations were conducted with an inter-particle friction coefficient  $\mu = 0.55$ , particle shear modulus  $G = 29$  GPa, and Poisson ratio  $\nu = 0.15$ . We used a scaling of the particles' material density, in the manner of Thornton [65], so that slow, quasi-static simulations could be completed with reasonable computation time.

As has been noted by Alonso-Marroquín et al. [16] and Froiio and Roux [21], DEM simulations necessarily involve a compromise between scientific intent and computational expedience. Without proper care, DEM simulations can yield results that are sensitive to strain rate, due to the particles' inertias and to the damping that is employed to stabilize the particles' motions [72]. Our intent was to model behavior in which these effects were minimized so that rate-independent behavior was attained. To this end, we used a slow strain rate (strain increments of  $1 \times 10^{-8}$  and minimal viscous damping (2% of critical damping)).

Several performance parameters were used to verify the quasi-static and rate-independent nature of these probes. The inertial number  $I = \dot{\epsilon} \sqrt{m/(pd)}$ , a relative measure of loading and inertial rates, was about  $1 \times 10^{-11}$ , signifying nearly quasi-static loading [73]. During the incremental probes, the average imbalance of force on a particle was less than 0.003% of the average contact force (parameter  $\chi$  in [74, 72]). The average kinetic energy of the particles was less than  $3 \times 10^{-7}$  times the elastic energy in the contacts. With the very slow strain rates of the simulations, doubling the strain increment from  $1 \times 10^{-8}$  to  $2 \times 10^{-8}$  had minimal effect on the monotonic stress-strain response. Boundary movements were regulated so that any six of the stress or strain components (or any six linear combination of these components) could be controlled at desired rates. When a stress component was controlled, it would typically remain on target to within 0.001 Pa, compared with the mean stress of 100 kPa and stress-probes that produced stress changes  $|d\sigma_{ij}|$  on the order of 100 Pa. As further verification of strain rate indifference during loading, we also conducted brief creep and stress relaxation tests in which either the stress or the assembly boundaries were frozen at the end of a stress probe. Froiio and Roux [21] have noted a tendency for an assembly to exhibit creep during small stress probes, an inclination that can obscure the probe results. During our creep tests, the strain rate was  $0.5\text{--}3 \times 10^{-10}$ , far less than the loading rate of  $1 \times 10^{-8}$ . During stress relaxation with zero strain rate, the stress changed at a rate of less than 4% of that typically measured during the incremental stress probes that were used in this study. The strain increment of  $2 \times 10^{-6}$  and strain steps of  $1 \times 10^{-8}$  entailed 200 steps. Although small fluctuations were noted in the first few steps, the advance of stress and strain were fairly uniform within the 200 strain steps. Moreover, the envelopes in Figs. 3–6 and 11 are quite smooth, even near the origin of these plots, where the strain parts are minuscule, and at high magnification, indicating that random errors are negligible. All of these measurements indicate that the behavior in the simulations was nearly quasi-static and independent of loading rate.

The DEM simulations were done with the authors' OVAL code (see [36]) and were run with a 4th generation Intel i7 processor on a single thread. The monotonic loading in Fig. 1, in which the strain was advanced to 16%, took 47 days of compute time; whereas, each probe in the series of Figs. 3 to 6 took about 6 minutes of compute time.

## References

- [1] Y. Yang, H. S. Yu, K. K. Muraleetharan, Solution existence conditions for elastoplastic constitutive models of granular materials, *Int. J. Plasticity* 21 (12) (2005) 2406–2425.
- [2] W. Wu, E. Bauer, D. Kolymbas, Hypoplastic constitutive model with critical state for granular materials, *Mech. of Mater.* 23 (1) (1996) 45–69.
- [3] J. Lin, W. Wu, R. I. Borja, Micropolar hypoplasticity for persistent shear band in heterogeneous granular materials, *Comput. Methods Appl. Mech. Eng.* 289 (2015) 24–43.
- [4] K. Hashiguchi, Generalized plastic flow rule, *Int. J. Plasticity* 21 (2) (2005) 321–351.
- [5] Q. Z. Zhu, J.-F. Shao, M. Mainguy, A micromechanics-based elastoplastic damage model for granular materials at low confining pressure, *Int. J. Plasticity* 26 (4) (2010) 586–602.
- [6] F. Nicot, F. Darve, The H-microdirectional model: accounting for a mesoscopic scale, *Mech. of Mater.* 43 (12) (2011) 918–929.
- [7] W.-C. Yeh, H.-Y. Lin, An endochronic model of yield surface accounting for deformation induced anisotropy, *Int. J. Plasticity* 22 (1) (2006) 16–38.
- [8] G. C. Ganzenmüller, S. Hiermaier, M. O. Steinhauser, Shock-wave induced damage in lipid bilayers: a dissipative particle dynamics simulation study, *Soft Matter* 7 (9) (2011) 4307–4317.
- [9] P. I. Lewin, J. B. Burland, Stress-probe experiments on saturated normally consolidated clay, *Géotechnique* 20 (1) (1970) 38–56.
- [10] F. Tatsuoka, K. Ishihara, Yielding of sand in triaxial compression, *Soils and Found.* 14 (2) (1974) 63–76.
- [11] J. P. Bardet, Observations on the effects of particle rotations on the failure of idealized granular materials, *Mech. of Mater.* 18 (2) (1994) 159–182.
- [12] A. Anandarajah, K. Sobhan, N. Kuganenthira, Incremental stress-strain behavior of granular soil, *J. Geotech. Eng.* 121 (1) (1995) 57–68.
- [13] P. Royis, T. Doanh, Theoretical analysis of strain response envelopes using incrementally non-linear constitutive equations, *Int. J. Numer. and Anal. Methods in Geomech.* 22 (2) (1998) 97–132. doi:10.1002/(SICI)1096-9853(199802)22:2<97::AID-NAG911>3.0.CO;2-Z.
- [14] Y. Kishino, On the incremental nonlinearity observed in a numerical model for granular media, *Revista Italiana Di Geotecnica* 3 (2003) 30–38.
- [15] F. Alonso-Marroquín, H. Herrmann, The incremental response of soils. an investigation using the discrete-element method, *J. Eng. Math.* 52 (1-3) (2005) 11–34.
- [16] F. Alonso-Marroquín, S. Luding, H. J. Herrmann, I. Vardoulakis, Role of anisotropy in the elastoplastic response of a polygonal packing, *Phys. Rev. E* 71 (5) (2005) 051304.
- [17] F. Calvetti, G. Viggiani, C. Tamagnini, A numerical investigation of the incremental behavior of granular soils, *Rivista Italiana di Geotecnica* 3 (2003) 11–29.
- [18] C. Tamagnini, F. Calvetti, G. Viggiani, An assessment of plasticity theories for modeling the incrementally nonlinear behavior of granular soils, *Journal of engineering mathematics* 52 (1-3) (2005) 265–291.
- [19] L. Sibille, F. Nicot, F. V. Donzé, F. Darve, Material instability in granular assemblies from fundamentally different models, *Int. J. Numer. and Anal. Methods in Geomech.* 31 (3) (2007) 457–481.
- [20] J.-P. Plassiard, N. Belheine, F.-V. Donzé, A spherical discrete element model: calibration procedure and incremental response, *Granul. Matter* 11 (5) (2009) 293–306.
- [21] F. Froiio, J.-N. Roux, Incremental response of a model granular material by stress probing with dem simulations, in: J. Goddard, P. Giovine, J. T. Jenkins (Eds.), *IUTAM-ISIMM Symposium on mathematical modeling and physical instances of granular flow*. AIP Conference Proceedings, Vol. 1227, AIP, 2010, pp. 183–197.
- [22] B. Harthong, R. G. Wan, Directional plastic flow and fabric dependencies in granular materials, in: *AIP Conference Proceedings*, Vol. 1542, 2013, pp. 193–196. doi:10.1063/1.4811900.
- [23] R. Wan, M. Pinheiro, On the validity of the flow rule postulate for geomaterials, *Int. J. Numer. and Anal. Methods in Geomech.* 38 (8) (2014) 863–880.
- [24] M. R. Kuhn, A. Daouadji, Quasi-static incremental behavior of granular materials: Elastic–plastic coupling and micro-scale dissipation, *J. Mech. Phys. Solids* 114 (2018) 219–237. doi:https://doi.org/10.1016/j.jmps.2018.02.019.
- [25] I. Agnolin, J.-N. Roux, Internal states of model isotropic granular packings. III. elastic properties, *Phys. Rev. E* 76 (2007) 061304.
- [26] T. Hueckel, Coupling of elastic and plastic deformations of bulk solids, *Meccanica* 11 (4) (1976) 227–235. doi:10.1007/BF02128296.
- [27] Y. F. Dafalias, Elasto-plastic coupling within a thermodynamic strain space formulation of plasticity, *Int. J. Non-linear Mech.* 12 (5) (1977) 327–337.
- [28] T. Hueckel, G. Maier, Incremental boundary value problems in the presence of coupling of elastic and plastic deformations: a rock mechanics oriented theory, *Int. J. Solids Struct.* 13 (1) (1977) 1–15.
- [29] I. F. Collins, G. T. Houslyby, Application of thermomechanical principles to the mod-

- elling of geotechnical materials, *Proc. R. Soc. Lond. A* 453 (1964) (1997) 1975–2001. arXiv:<http://rspa.royalsocietypublishing.org/content/453/1964/1975.full.pdf>.
- [30] M. Pastor, O. C. Zienkiewicz, A generalized plasticity, hierarchical model for sand under monotonic and cyclic loading, in: *Proc., 2nd Int. Symp. on Numerical Models in Geomechanics*, Jackson and Son, Ghent, Belgium, 1986, pp. 131–150.
- [31] R. Hill, The essential structure of constitutive laws for metal composites and polycrystals, *J. Mech. Phys. Solids* 15 (2) (1967) 79–95.
- [32] M. Khojastehpour, Y. Murakami, K. Hashiguchi, Antisymmetric bifurcation in an elastoplastic cylinder with tangential plasticity, *Mech. of Mater.* 38 (11) (2006) 1061–1071.
- [33] M. R. Kuhn, OVAL and OVALPLOT: programs for analyzing dense particle assemblies with the Discrete Element Method, <http://faculty.up.edu/kuhn/oval/oval.html>.
- [34] M. O. Steinhauser, K. Grass, E. Strassburger, A. Blumen, Impact failure of granular materials—non-equilibrium multiscale simulations and high-speed experiments, *Int. J. Plasticity* 25 (1) (2009) 161–182.
- [35] S. Chakraborty, A. Shaw, A pseudo-spring based fracture model for sph simulation of impact dynamics, *Int. J. Impact Engrg.* 58 (2013) 84–95.
- [36] M. R. Kuhn, H. Renken, A. Mixsell, S. Kramer, Investigation of cyclic liquefaction with discrete element simulations, *J. Geotech. and Geoenv. Eng.* 140 (12) (2014) 04014075. doi:10.1061/(ASCE)GT.1943-5606.0001181.
- [37] M. R. Kuhn, K. Bagi, Specimen size effect in discrete element simulations of granular assemblies, *J. Eng. Mech.* 135 (6) (2009) 485–492.
- [38] R. Mindlin, H. Deresiewicz, Elastic spheres in contact under varying oblique forces, *J. Appl. Mech.* 19 (1) (1953) 327–344.
- [39] M. R. Kuhn, Implementation of the Jäger contact model for discrete element simulations, *Int. J. Numer. Methods Eng.* 88 (1) (2011) 66–82.
- [40] D. Elata, J. G. Berryman, Contact force-displacement laws and the mechanical behavior of random packs of identical spheres, *Mech. of Mater.* 24 (3) (1996) 229–240.
- [41] F. Nicot, F. Darve, On the elastic and plastic strain decomposition in granular materials, *Granul. Matter* 8 (3–4) (2006) 221–237. doi:10.1007/s10035-006-0012-4. URL <http://dx.doi.org/10.1007/s10035-006-0012-4>
- [42] T. Hueckel, R. Nova, Some hysteresis effects of the behaviour of geologic media, *Int. J. Solids Struct.* 15 (8) (1979) 625–642.
- [43] M. Pouragha, R. Wan, Non-dissipative structural evolutions in granular materials within the small strain range, *Int. J. Solids Struct.* 110–111 (2017) 94–105.
- [44] M. Pouragha, R. Wan, On elastic deformations and decomposition of strain in granular media, *Int. J. Solids Struct.*
- [45] L. Rendulic, Relation between void ratio and effective principal stresses for a remolded silty clay, in: *Proc. of 1st Int. Conf. on Soil Mechanics and Foundation Engineering*, Vol. 3, Harvard University Press, Cambridge, MA, 1936, pp. 48–51.
- [46] G. Gudehus, D. Kolymbas, A constitutive law of rate type for soils, in: W. Wittke (Ed.), *Numerical Methods in Geomechanics Aachen 1979*, Vol. 1, A. A. Balkema, Rotterdam, 1979, pp. 319–329.
- [47] F. Darve, F. Nicot, On flow rule in granular media: phenomenological and multi-scale views (Part II), *Int. J. Numer. and Anal. Methods in Geomech.* 29 (14) (2005) 1411–1432.
- [48] R. Hill, Some basic principles in the mechanics of solids without a natural time, *J. Mech. Phys. Solids* 7 (3) (1959) 209–225.
- [49] F. Darve, The expression of rheological laws in incremental form and the main classes of constitutive equations, in: F. Darve (Ed.), *Geomaterials: constitutive equations and modelling*, Elsevier, London, 1990, pp. 123–147.
- [50] O. C. Zienkiewicz, Z. Mroz, Generalized plasticity formulation and applications to geomechanics, in: C. S. Desai, R. H. Gallagher (Eds.), *Mechanics of engineering materials*, Vol. 44, Wiley, New York, 1984, pp. 655–680.
- [51] K. Hashiguchi, Fundamental requirements and formulation of elastoplastic constitutive equations with tangential plasticity, *Int. J. Plasticity* 9 (5) (1993) 525–549.
- [52] Y. Lai, M. Liao, K. Hu, A constitutive model of frozen saline sandy soil based on energy dissipation theory, *Int. J. Plasticity* 78 (2016) 84–113.
- [53] J. W. Rudnicki, J. R. Rice, Conditions for the localization of deformation in pressure-sensitive dilatant materials, *J. Mech. Phys. Solids* 23 (1975) 371–394.
- [54] F. Darve, F. Nicot, On incremental non-linearity in granular media: phenomenological and multi-scale views (part i), *Int. J. Numer. and Anal. Methods in Geomech.* 29 (14) (2005) 1387–1409.
- [55] P.-Y. Hicher, C. S. Chang, A microstructural elastoplastic model for unsaturated granular materials, *Int. J. Solids Struct.* 44 (7-8) (2007) 2304–2323.
- [56] S. Iai, T. Tobita, O. Ozutsumi, K. Ueda, Dilatancy of granular materials in a strain space multiple mechanism model, *Int. J. Numer. and Anal. Methods in Geomech.* 35 (3) (2011) 360–392.
- [57] A. Tordesillas, M. Muthuswamy, S. D. C. Walsh, Mesoscale measures of nonaffine deformation in dense granular



- assemblies, *J. Eng. Mech.* 134 (12) (2008) 1095–1113.
- [58] M. R. Kuhn, Maximum disorder model for dense steady-state flow of granular materials, *Mech. of Mater.* 93 (2016) 63–80.
- [59] M. R. Kuhn, Contact transience during slow loading of dense granular materials, *J. Eng. Mech.* (2016) C4015003doi:10.1061/(ASCE)EM.1943-7889.0000992.
- [60] S. Pietruszczak, A flow theory for soil: Concept of multiple neutral loading surfaces, *Comput. and Geotech.* 2 (3) (1986) 185–203.
- [61] A. Anandarajah, Multi-mechanism anisotropic model for granular materials, *Int. J. Plasticity* 24 (5) (2008) 804–846.
- [62] J. Mandel, Généralisation de la théorie de plasticité de WT Koiter, *Int. J. Solids Struct.* 1 (3) (1965) 273–295.
- [63] P. A. Cundall, O. D. L. Strack, A discrete numerical model for granular assemblies, *Géotechnique* 29 (1) (1979) 47–65.
- [64] M. R. Kuhn, J. K. Mitchell, Modelling of soil creep with the discrete element method, *Eng. Comput.* 9 (2) (1992) 277–287.
- [65] C. Thornton, Numerical simulations of deviatoric shear deformation of granular media, *Géotechnique* 50 (1) (2000) 43–53.
- [66] L. Vu-Quoc, X. Zhang, O. R. Walton, A 3-D discrete-element method for dry granular flows of ellipsoidal particles, *Comput. Methods Appl. Mech. Eng.* 187 (3) (2000) 483–528.
- [67] J. F. Favier, M. H. Abbaspour-Fard, M. Kremmer, Modeling nonspherical particles using multisphere discrete elements, *J. Eng. Mech.* 127 (10) (2001) 971–977.
- [68] K. Arulmoli, K. K. Muraleetharan, M. M. Hossain, L. S. Fruth, VELACS verification of liquefaction analyses by centrifuge studies laboratory testing program soil data report, Tech. Rep. Project No. 90-0562, The Earth Technology Corporation, Irvine, CA, data available through <http://yees.usc.edu/velacs> (1992).
- [69] C. Thornton, C. W. Randall, Applications of theoretical contact mechanics to solid particle system simulation, in: M. Satake, J. Jenkins (Eds.), *Micromechanics of Granular Materials*, Elsevier Science Pub. B.V., Amsterdam, The Netherlands, 1988, pp. 133–142.
- [70] P. A. Cundall, Computer simulations of dense sphere assemblies, in: M. Satake, J. Jenkins (Eds.), *Micromechanics of Granular Materials*, Elsevier Science Pub. B.V., Amsterdam, The Netherlands, 1988, pp. 113–123.
- [71] X. Lin, T.-T. Ng, A three-dimensional discrete element model using arrays of ellipsoids, *Géotechnique* 47 (2) (1997) 319–329.
- [72] K. Suzuki, M. R. Kuhn, Uniqueness of discrete element simulations in monotonic biaxial shear tests, *Int. J. Geomech.* 14 (5) (2014) 06014010. doi:10.1061/(ASCE)GM.1943-5622.0000365.
- [73] F. da Cruz, S. Emam, M. Prochnow, J.-N. Roux, F. Chevoir, Rheophysics of dense granular materials: Discrete simulation of plane shear flows, *Phys. Rev. E* 72 (2) (2005) 021309.
- [74] T.-T. Ng, Input parameters of discrete element methods, *J. Eng. Mech.* 132 (7) (2006) 723–729.